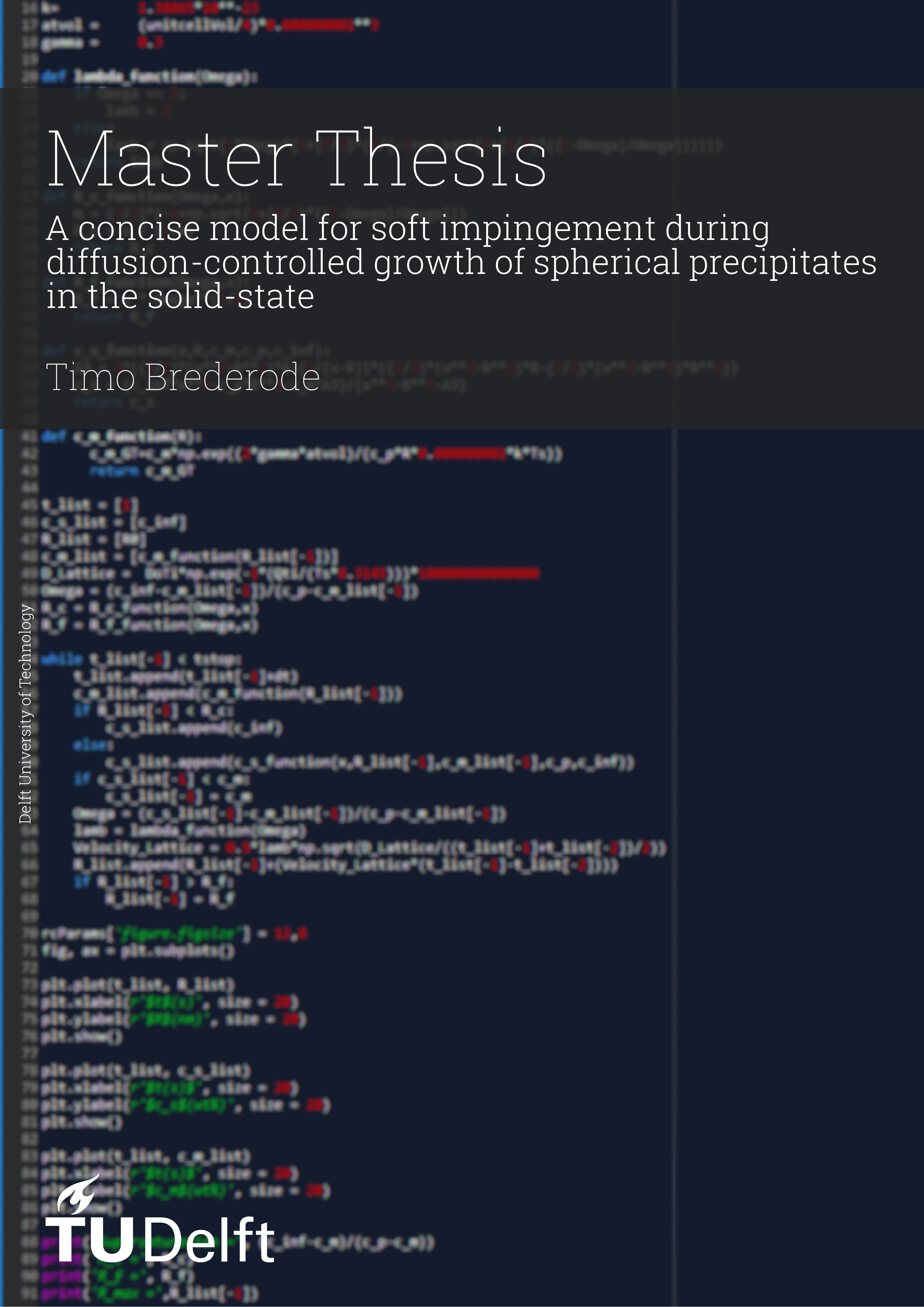

Master Thesis

A concise model for soft impingement during diffusion-controlled growth of spherical precipitates in the solid-state

Timo Brederode

Delft University of Technology

Master Thesis

A concise model for soft impingement during diffusion-controlled growth of spherical precipitates in the solid-state

by

Timo Brederode

to obtain the Master of Science (M.Sc.) degree in Materials Science and Engineering
at the Delft University of Technology,
to be defended publicly on Monday March 26, 2025 at 10 AM.

Student number:	4979133	
Project duration:	September 2, 2024 – March 1, 2025	
Thesis committee:	Dr. Ir. Erik Offerman,	TU Delft (MSE), supervisor
	Dr. Pina Mecozzi,	TU Delft (MSE), supervisor
	Prof. Dr. Maria Santofimia Navarro,	TU Delft (MSE)
	Dr. Ir. Niels van Dijk	TU Delft (FAME)

Acknowledgements

With this thesis, my years at the master Materials Science and Engineering will come to an end. I have greatly enjoyed my time obtaining my master's degree and have discovered my passion and interests for metals. I am very grateful for the opportunity to work on modelling soft impingement for precipitation growth and to be able to design my own model.

First and foremost, I would like to thank my supervisors, Dr. Ir. Erik Offerman and Dr. Pina Mecozzi, for supporting me with the thesis work. I greatly appreciate our regular discussions, which were invaluable for my personal growth and for keeping me on track to graduate. A special thanks to Dr. Pina Mecozzi for proof reading and improving the quality of the thesis work.

Furthermore, I would like to thank my parents for their love and support, which have helped me achieve my academic goals. Additionally, thanks to Manon for her constant encouragement and little Groot for his companionship.

Abstract

The effect of soft impingement is modelled for the isothermal, diffusion-controlled growth of spherical precipitates in the solid-state. A two-stage soft impingement phase, isotropic growth in 3D and site saturation are assumed, which lead to a mean field approach for soft impingement. A mass balance is used in combination with a non-linear concentration profile approximation [1], instead of the ordinary linear concentration profile [2][3][4], to improve the description of growth under conditions of overlapping diffusion fields and low supersaturation. In addition, the capillary effects, dislocation assisted growth via pipe diffusion, and boundary assisted growth via boundary diffusion are discussed. The model has been applied to the growth of TiC-precipitates during tempering of a quenched Fe-C-Mn-Ti steel. The results are in good agreement with published experimental data of precipitate growth [2].

Contents

Acknowledgements **ii**

Abstract **iv**

1 Basics of Modeling Precipitation **1**
- 1.1 Precipitation Hardening 1
- 1.2 Modeling Particle Growth 1
  - 1.2.1 Diffusion-Controlled Growth 1
  - 1.2.2 Exact Solution 2
  - 1.2.3 Approximations 3
- 1.3 Introducing Soft Impingement 6
- 1.4 Introducing Additional Effects 6

2 Soft Impingement Model **7**
- 2.1 Model Description 7
- 2.2 Assumptions 7
- 2.3 Concentration Profiles 9
- 2.4 Start of Soft Impingement (R_c) 9
- 2.5 End of Growth (R_f) 11
- 2.6 Growth during Soft Impingement (c_s) 11
- 2.7 Model Summary 13

3 Additional Effects **15**
- 3.1 Gibbs Thomson Effect 15
- 3.2 Assisted Growth Models 15
  - 3.2.1 Single Dislocation Model 16
  - 3.2.2 Single Boundary Model 17
  - 3.2.3 Use of apparent diffusivities to describe high-diffusivity paths 18
- 3.3 Model Summary Including Additional Effects 20

4 Application and Discussion **21**
- 4.1 Input data 21
- 4.2 Concentration profile effect excluding soft impingement 22
- 4.3 Concentration profile effect including soft impingement 23
- 4.4 Application of the Gibbs Thomson effect 24
- 4.5 Application of the assisted growth models 26
  - 4.5.1 Multi dislocation model 26
  - 4.5.2 Single dislocation model 28
  - 4.5.3 Multi boundary model 30
  - 4.5.4 Single boundary model 31
- 4.6 Application for TiC precipitation in martensitic steel [2] 34
  - 4.6.1 Experimental data [2] 34
  - 4.6.2 Model comparison [2] 36
  - 4.6.3 Limitations of the model 38

5 Conclusion and Recommendations **41**

References **43**

A Appendix **45**
- A.1 Calculation for R_f 45
- A.2 Calculations for c_s 46
  - A.2.1 Linear concentration profile 46
  - A.2.2 Parabolic concentration profile 47
  - A.2.3 Non-linear concentration profile 48
- A.3 Gibbs Thomson Effect 48
- A.4 Single Dislocation Model 50

A.5 Boundary Assisted Growth Model 51

1

Basics of Modeling Precipitation

In this chapter, we will introduce the basics of precipitation hardening and modeling of diffusion-controlled growth to provide a basic understanding of this thesis work. The exact solution and different concentration profile approximations will be introduced. We will compare the exact solution and the concentration profile approximations to indicate the importance of using a new concentration profile approximation instead of the widely used linear concentration profile approximation. Next, we will introduce soft impingement and additional effects to particle growth. Here, we will discuss available soft impingement models and express the need for the model introduced in this thesis work.

1.1. Precipitation Hardening

Precipitation hardening is the process in which, during a heat treatment, supersaturated solutes will form small particles, called precipitates. The newly formed particles can act as barriers for the movement of dislocations, increasing the yield strength of the material. If enough stress is applied, the dislocations can cut through the particle or bow around the particle, leaving a dislocation loop. Whether the dislocation cuts or bows depend on the precipitate size [5]. This can be seen in Figure 1.1.

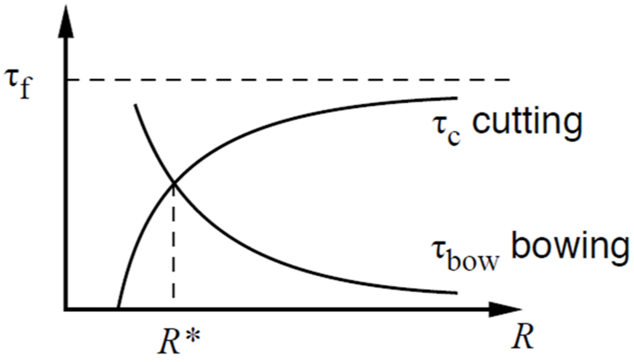

Figure 1.1: Competition between cutting and bowing [5].

It can be seen that the smaller the precipitate, the easier it is to cut through it. For large precipitates, it is easier to bow around it, since the distance between large precipitates is usually higher than that of smaller ones. Thus, there is an optimal size for the precipitate, which resists cutting and bowing as much as possible, given the radius R^*. For this reason, it is important to be able to model the growth of the precipitates. If we understand the growth mechanics of the precipitates, then we can modify the production method to obtain an optimal size of the precipitate, which gives the best properties to the material.

1.2. Modeling Particle Growth

1.2.1. Diffusion-Controlled Growth

To be able to model the growth or precipitates, we will have to make use of some assumptions. First, we assume that the precipitate is a spherical particle. Next, we assume diffusional growth. This means that the growth kinetics are controlled by the substituted solute diffusion in the parent matrix. The reason for this is that the precipitates form from diffusion of alloying elements, which are located at substitutional lattice sites. The diffusion of these elements is very slow, compared to elements located at interstitial sites. We also assume this particle to be alone in an infinitely large lattice. Our starting point, to describe the diffusion-controlled growth problem, is the concentration profile of the solute at the particle, this can be seen in Figure 1.2. The center of the particle is at distance 0 and R is the radius. c^p, c^m and c^∞ are the solute concentration in the particle, in the matrix at the side of the interface and in the matrix far away from the particle respectively. For c^p and c^m, we take the equilibrium solute concentrations given by the phase diagram. c^∞ is given by the measured solute concentration in the matrix. We assume a stoichiometric composition in the particle. Throughout the whole particle the concentration is constant at c^p. In addition, the concentration of solute in the matrix at the particle interface approaches the equilibrium value with the particle phase according to the phase diagram c^m. In the Figure also mentioned is Ω, supersaturation is given as the relationship between the difference in the solute concentration in the matrix and the interphase ($c^\infty - c^m$) and the difference in the solute concentration in the particle and the interphase ($c^p - c^m$). The term Ω will come back frequently, as the growth rate depends on it.

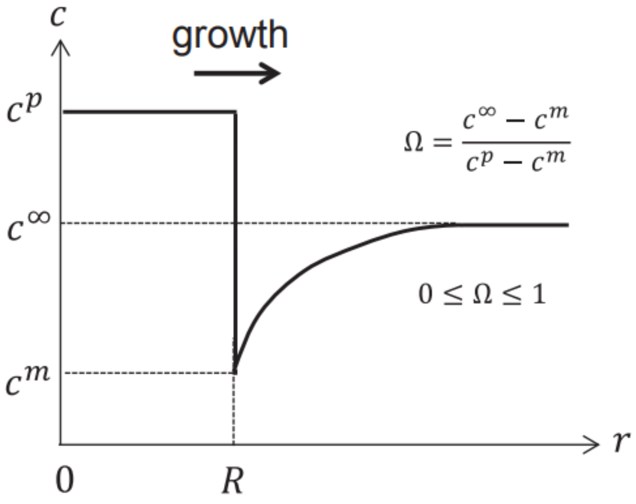

Figure 1.2: The solute concentration profile [1].

1.2.2. Exact Solution

The exact solution was first produced by Dubé et al [6] and more recently reproduced by Hubert et al [7]. From Zener [8], it shows that from dimensional arguments the particle radius is given by

$$R = \lambda\sqrt{Dt} \tag{1.1}$$

Where here D is the diffusion coefficient of the solute in the matrix, t is time and λ is the parabolic growth constant. λ is a function of the solute concentrations c^p, c^m and c^∞, usually by being a function of Ω. For the given problem, two equations can be set. The flux of the solute atoms that will move away from the interface. This equation is given by Fick's law.

$$F_1 = -D\frac{\delta c}{\delta r}\bigg|_R \tag{1.2}$$

Where $(\delta c/\delta x)_R$ is the concentration gradient of the solute in the matrix near the interphase. Next, the flux of the atoms that will enter the precipitate due to the movement of the interphase is given by

$$F_2 = (c^m - c^p)\frac{dR}{dt} \tag{1.3}$$

Here R is the position of the interface of the particle and dR/dt is the rate of growth. If no accumulations of the solute is present at the particle interface, then equation (1.2) and (1.3) must be equal. This is called the flux balance equation.

$$F_1 = F_2 \tag{1.4}$$

$$(c^m - c^p)\frac{dR}{dt} = -D\frac{\delta c}{\delta r}\bigg|_R \tag{1.5}$$

Fick's second law is used to get an equation for the solute concentration profile. For a spherical particle, this is given by

$$\frac{dc}{dt} = D(\frac{d^2c}{dx^2} + \frac{d^2c}{dy^2} + \frac{d^2c}{dz^2}) \tag{1.6}$$

Considering polar coordinates and assuming isotropic diffusion (no vary in θ and ϕ). Equation (1.6) changes to

$$\frac{dc}{dt} = D(\frac{d^2c}{dr^2} + \frac{2}{r}\frac{dc}{dr}) \tag{1.7}$$

Solving equation (1.5) and (1.7) gives the exact solution of the concentration profile as

$$c(r,t)^{3D} = c^{\infty} + \frac{1}{2}(c^m - c^p)\lambda^3 exp(\frac{\lambda^2}{4})(\frac{1}{r}exp(-\frac{r^2}{4Dt}\sqrt{Dt}) - \frac{\sqrt{\pi}}{2}erfc(\frac{r}{2\sqrt{Dt}})) \tag{1.8}$$

And the parabolic growth constant (λ) in 3D as

$$\frac{1}{2}\lambda^2(1 - \frac{\sqrt{\pi}}{2}\lambda \exp(\frac{\lambda^2}{4})erfc(\frac{\lambda}{2})) = \Omega \tag{1.9}$$

The exact solution give a relationship between λ and Ω. This is a transcendental equation. It is not possible to express λ as Ω due to the error function in equation (1.9). Thus is it not possible to express

$$R = f(\Omega, t) \tag{1.10}$$

This gives rise to the use of approximations. The available approximations are either made by simplifying either the diffusion equations (1.2) and (1.3) under specific assumptions, examples are the invariant size and invariant field approximation [9][10], or by the concentration profile in Figure 1.2, examples are the linear, parabolic or "modified linear" concentration profiles [1][3][4]. The terminology for the "modified linear" concentration profiles comes from the function of the concentration profile, where the 1D linear concentration profile has been modified to work for all values of Ω in 3D. This can be confusing, as the concentration profile is not linear itself. We will from here on refer to the non-linear concentration profile when we mention the approximation. For the use of our model, we will only focus on the concentration profile approximations.

1.2.3. Approximations

Linear concentration profile approximation [3]

The linear concentration profile approximation is illustrated in Figure 1.3.

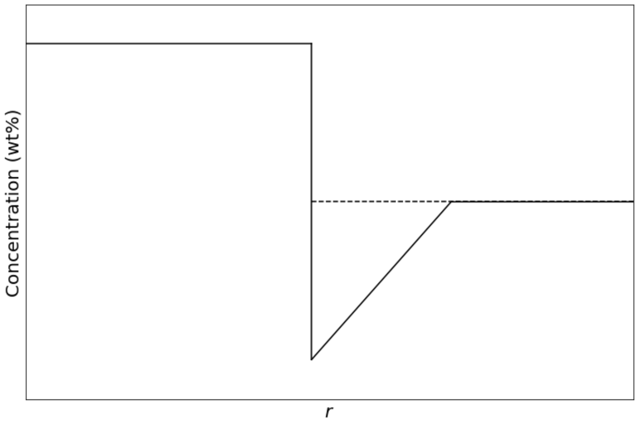

Figure 1.3: The solute concentration profile, assuming a linear concentration profile.

The concentration profile is given as

$$c(r,t) = \frac{c^{\infty} - c^m}{L}(r - R(t)) + c^m \tag{1.11}$$

Where L is the diffusion length, given by the distance between the particle interface and the end of the concentration gradient where the concentrations becomes constant. To get an expression for L, the following mass balance is solved

$$\int_0^R c^p 4\pi r^2 dr + \int_R^{R+L} c(r,t) 4\pi r^2 dr = \int_0^{R+L} c^{\infty} 4\pi r^2 dr \tag{1.12}$$

This gives

$$L = (\frac{1}{3}(44 + 54B + 6\sqrt{54 + 132B + 81B^2})^{\frac{1}{3}} - \frac{2}{3(44 + 54B + 6\sqrt{54 + 132B + 81B^2})^{\frac{1}{3}}} - \frac{4}{3})R \tag{1.13}$$

Where $B = \frac{c^\infty - c^p}{c^m - c^\infty} = \frac{1}{\Omega} - 1$. To get an expression for λ in $R = \lambda\sqrt{Dt}$, the following flux balance equation is used

$$(c^m - c^p)\frac{dR}{dt} = -D\frac{\delta c}{\delta r}\bigg|_R \tag{1.14}$$

This gives

$$\lambda = \frac{\sqrt{2\Omega}}{(\frac{1}{3}(44 + 54B + 6\sqrt{54 + 132B + 81B^2})^{\frac{1}{3}} - \frac{2}{3}(44 + 54B + 6\sqrt{54 + 132B + 81B^2})^{-\frac{1}{3}} - \frac{4}{3})^{\frac{1}{2}}} \tag{1.15}$$

Parabolic concentration profile approximation [4]

The parabolic concentration profile approximation is illustrated in Figure 1.4.

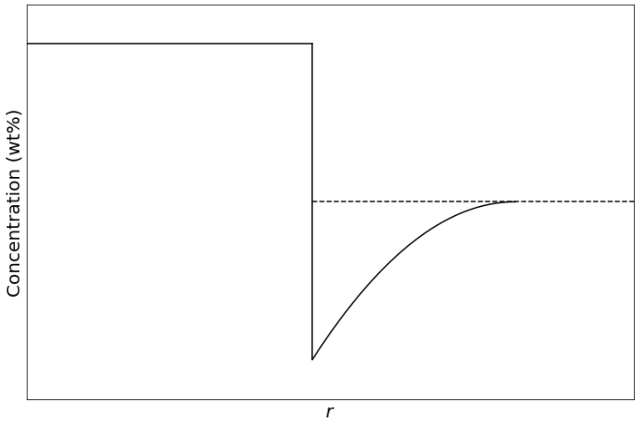

Figure 1.4: The solute concentration profile, assuming a parabolic concentration profile.

The concentration profile is given as

$$c(r,t) = c^m - 2\frac{c^\infty - c^m}{L}(r - R(t)) + \frac{c^\infty - c^m}{L^2}(r - R(t))^2 \tag{1.16}$$

L is calculated using the mass balance form eq (1.12).

$$L = (\frac{1}{3}\sqrt[3]{5}(20 + 27B + 3\sqrt{3}\sqrt{15 + 40B + 27B^2})^{\frac{1}{3}} - \frac{\sqrt[3]{25}}{3(20 + 27B + 3\sqrt{3}\sqrt{15 + 40B + 27B^2})^{\frac{1}{3}}} - \frac{5}{3})R \tag{1.17}$$

Where $B = \frac{c^\infty - c^p}{c^m - c^\infty} = \frac{1}{\Omega} - 1$. To get an expression for λ in $R = \lambda\sqrt{Dt}$, the flux balance from equation (1.14) is used, this gives

$$\lambda = \frac{2\sqrt{3}\Omega^{-\frac{1}{2}}}{(\sqrt[3]{5}(20 + 27B + 3\sqrt{3}\sqrt{15 + 40B + 27B^2})^{\frac{1}{3}} - \sqrt[3]{25}(20 + 27B + 3\sqrt{3}\sqrt{15 + 40B + 27B^2})^{-\frac{1}{3}} - 5)^{\frac{1}{2}}} \tag{1.18}$$

Non-linear concentration profile approximation [1]

The non-linear concentration profile approximation is illustrated in Figure 1.5.
The concentration profile is given as

$$c(r,t) = (c^m - c^\infty)\frac{R}{r}(1 - \frac{r - R}{L}) + c^\infty \tag{1.19}$$

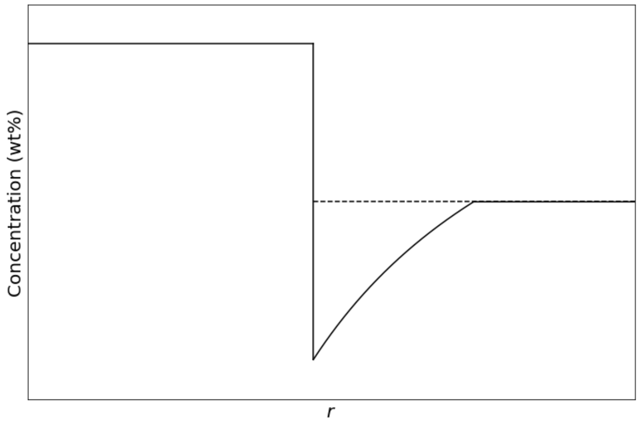

Figure 1.5: The solute concentration profile, assuming a non-linear concentration profile.

L is calculated using the mass balance form eq (1.12).

$$L = (\frac{3}{2}(-1 + \sqrt{1 + \frac{8}{9}(\frac{1-\Omega}{\Omega})}))R \tag{1.20}$$

To get an expression for λ in $R = \lambda\sqrt{Dt}$, the flux balance from equation (1.14) is used, this gives

$$\lambda = \sqrt{2\Omega(1 + \frac{2}{3}\frac{1}{-1 + \sqrt{1 + \frac{8}{9}(\frac{1-\Omega}{\Omega})}})} \tag{1.21}$$

Comparing the concentration profile approximations

To test the validity of the different concentration profile approximations, we will compare the resulting parabolic growth constant (λ) with that of the exact solution. This can be seen in Figures 1.6 and 1.7.

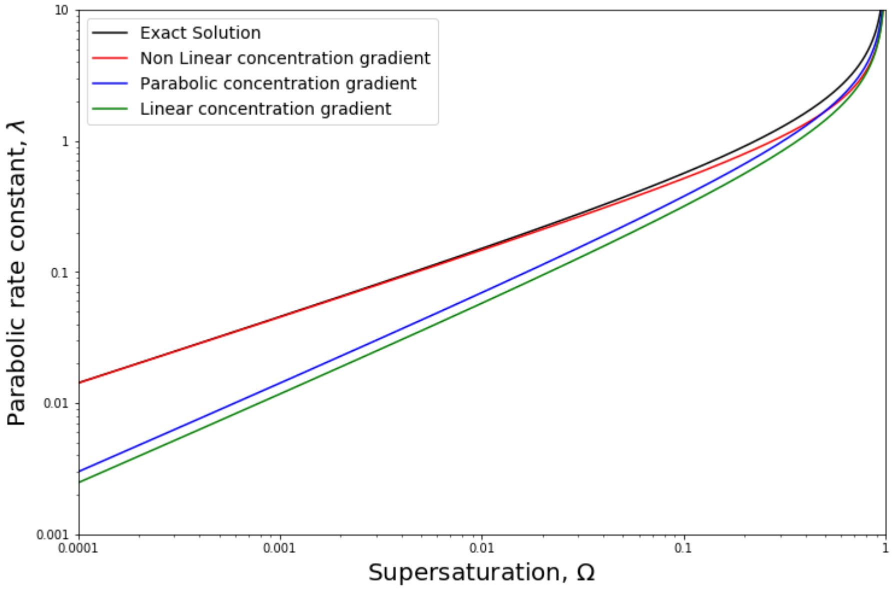

Figure 1.6: A comparison of λ for the exact solution and the concentration profile approximations.

From Figures 1.6 and 1.7, it can be seen that the linear and parabolic concentration profile approximation perform poorly at low Ω compared to that of the non-linear concentration profile approximation. All concentration profile approximations seem to perform well at higher Ω. To be exact, the non-linear concentration profile approximation performs best at $\Omega < 0.486$, and the parabolic concentration profile approximation at $\Omega > 0.486$.

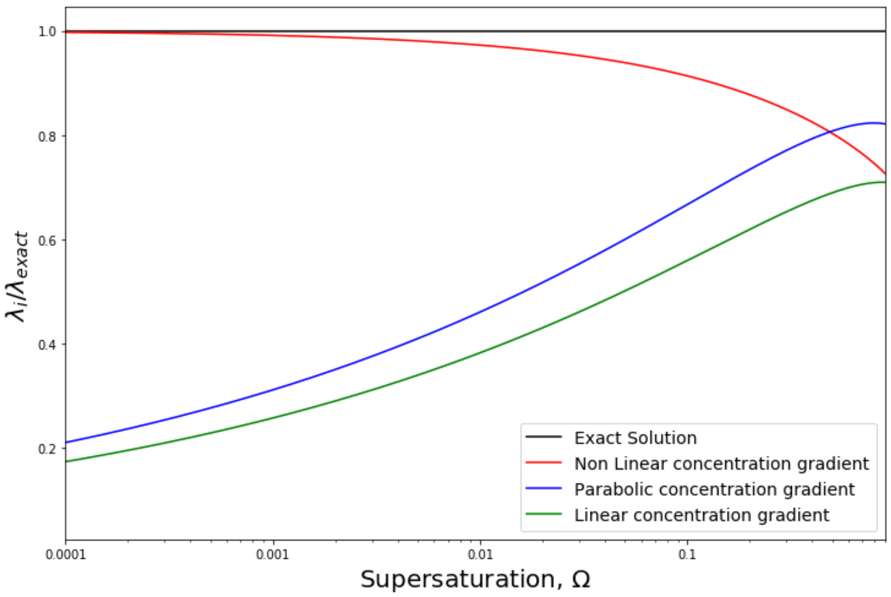

Figure 1.7: A comparison of λ for the exact solution and the concentration profile approximations. Normalized to λ of the exact solution.

1.3. Introducing Soft Impingement

Soft impingement is an effect that slows precipitate growth due to overlapping concentration profiles. Usually, growth occurs in two stages [3][4]. The first stage is where there is no overlap in the concentration profile of different precipitates. In the second stage, the concentration profiles of different precipitates will start to overlap and reduce the growth rate. We now remove the assumption made earlier that there is only a single precipitate. The second stage includes overlap of the solute concentration profiles of the initial and neighboring particles. Many soft impingement models are available [3][4][11][12][13]. Most models focus only on the linear concentration profile [3][11][12][13][14]. Chang et al. [4] also include other polynomial functions, like the parabolic concentration profile, but only focuses on 1D soft impingement and Fang et al. [14] introduced a 3D mixed-mode model and focused on the parabolic concentration profile. We saw in Figure 1.6 and 1.7 that the linear and parabolic concentration profile approximation perform less accurate at lower supersaturation. This shows that there is a gap in the literature for an accurate soft impingement model for low supersaturation, which is usually the case for precipitation. This thesis work aims to apply the new 'modified' linear or non-linear concentration profile for the design of a new soft impingement model which will accurately predict particle growth for precipitation but is also valid at all values for Ω. This thesis also aims so address the difference between the non-linear and the poly nominal concentration profile approximations to validate the use of the non-linear concentration profile approximation. The soft impingement models will be introduced in **Chapter 2** and its application will be discussed in **Chapter 4**. All the calculations for the model design are available in the appendix.

1.4. Introducing Additional Effects

Besides the design of a soft impingement model with the non-linear concentration profile approximation, this thesis also introduces additional effects to the particle growth like the Gibbs Thomson effect, which accounts for the change in equilibrium concentration at the interface of the particle due to interfacial energies, and assisted growth effects, which account for highly diffusive paths like dislocations and boundaries. The additional effects will be introduced separately of the soft impingement model design in **Chapter 3** and will be discussed in **Chapter 4**.

2

Soft Impingement Model

In this chapter, we will first explain the basis of the model. We will list and validate all the assumptions used in the soft impingement model. Next, we will talk about three concentration profiles that we will apply the model to. Namely, the widely used linear concentration profile, the parabolic concentration profile and a non-linear concentration profile. We will preform the 3D mass balance on the given concentration profiles to calculate the start of soft impingement, end of soft impingement, and growth during soft impingement. We will end the chapter with a summary and flow chart of the model.

2.1. Model Description

The diffusional growth model is based on the work of Chen et al. [4]. For the assumption of diffusional growth, a one-dimensional mass balance was used to account for the effect of soft impingement. Chen et al. applied the model to the austenite to ferrite transformation. The assumption of one dimension is valid for this case, since the 'particle', in this case ferrite, is large enough to assume a planar interface. The one-dimensional assumption becomes invalid for the case of smaller particles, such as precipitation of alloy carbides in steel. In this case, it is more accurate to assume a spherical particle. As a result of the problem being thee-dimensional, the mass balance will change, as will be seen in this chapter. In addition, Chen et al. worked with a polynomial function of the concentration profile. Here we will include a non-polynomial function for the concentration profile to improve the model at low supersaturation.

The 3D soft impingement model is based on the following mass balance.

$$\int_0^R c^p 4\pi r^2 dr + \int_R^x c(r,t,c_s) 4\pi r^2 dr = \int_0^x c_0^\infty 4\pi r^2 dr \tag{2.1}$$

Where x is half the distance from the center of the initial particle to the neighboring particle, c_0^∞ is the solute concentration in the matrix, far away from the particle, before soft impingement and c_s is the solute concentration at $r = x$. A visualization of the model, using the linear concentration profile approximation, can be seen in Figure 2.1. The gray area under the function represents the left side of the mass balance equation. The right side represents the mass over the same volume before nucleation.

2.2. Assumptions

We need some assumptions to be able to model the growth of precipitates. Below is a summary of all the assumptions and their validation used in the model of which most are already mentioned:

- **The precipitate is a spherical particle ($V_{particle} = \frac{4}{3}\pi r^3$):**
  Precipitates can be assumed spherical since this is the optimal morphology due to the smallest area over volume ratio. Especially for small particles, because their ratio is highest.
- **Growth of the particle is diffusion-controlled ($R = f(D, t, \Omega)$):**
  The growth or precipitates can be assumed to be controlled by diffusion since precipitates contain alloying elements located at substitutional lattice sites, which means that diffusion will occur through vacancy diffusion and is very slow compared to elements at interstitial lattice sites.

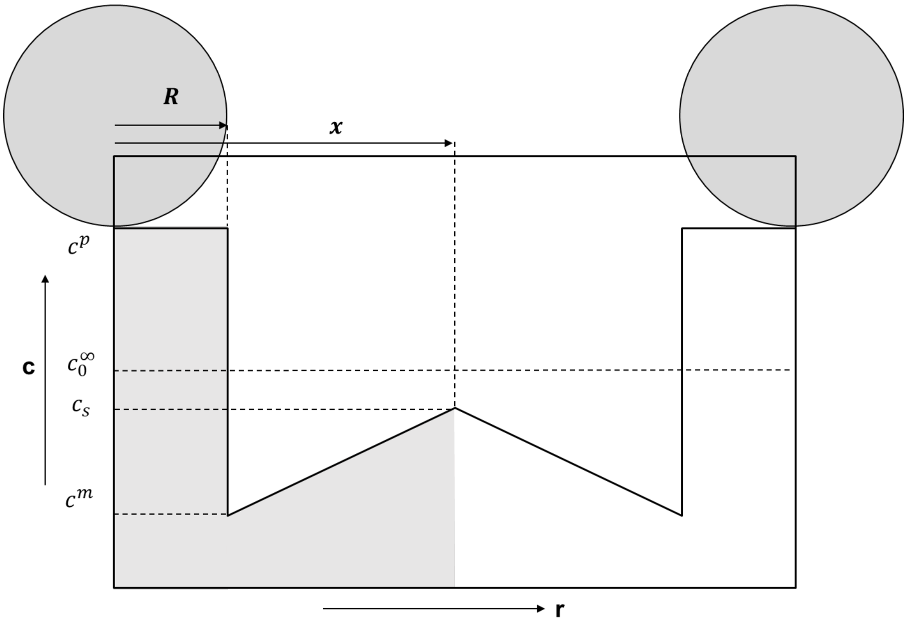

Figure 2.1: Model for growth of particles using the linear concentration profile approximation. c^p is the solute concentration in the particle, c_0^∞ far away from the particle before soft impingement, c^m is the solute concentration in the matrix at the interface of the particle, c_s is the solute concentration at $r = x$, R is the particle radius and x is half the distance from the center of the initial particle to the neighboring particle.

- **The particle has stoichiometric composition (c^p = constant):**
  To simplify the mathematics, we assume that the concentration in the particle is constant from the center until the interface.
- **All particles nucleate at the same time ($R_1 = R_2$, $L_1 = L_2$):**
  If nucleation rate is high, we can assume that all particles nucleate at the same time. The initial particle will have the same size and diffusion length as the neighboring particle.
- **Uniform distribution of particles (x)**
  Every particle has its neighboring particle at the same distance. The distance from the center of the initial particle to the middle of the initial and neighboring particle is x.
- **Soft impingement occurs in two stages:**
  The first stage includes non-overlapping concentration profiles and the second stage includes overlapping concentration profiles.
- **No hard impingement:**
  We assume that the particle will not reach a surface or second phase that forces growth to slow down or stop.

In addition to the assumptions mentioned, we will include some assumptions in the soft impingement model, which will be removed in **Chapter 3**, where we discuss additional effects on the growth of particles:

- **No capillary effects or "Gibbs Thomson Effect" (c^m = constant equilibrium concentration):**
  The concentration at in the matrix at the particle interface will be at the concentration according to the phase diagram taken from Thermo-Calc. The interfacial energy of the particle will not affect the equilibrium concentration.
- **No dislocations or boundaries:**
  No defects are present that can act as highly diffusive paths, such as dislocations or boundaries.

2.3. Concentration Profiles

As mentioned, we will use the linear, parabolic and non-linear concentration profile. A summary of the concentration profiles and their dependence on L and R is given in Table 2.1. Here, $c_i(r,t)$ is the concentration profile of the initial particle for values of r in the range $R < r < (R + L)$.

Linear concentration profile $c_i(r,t) = \frac{c^\infty - c^m}{L}(r - R(t)) + c^m$	$L_{lin}(\Omega) = (\frac{1}{3}(A_{lin})^{\frac{1}{3}} - \frac{2}{3(A_{lin})^{\frac{1}{3}}} - \frac{4}{3})R$ $A_{lin} = 44 + 54B + 6\sqrt{54 + 132B + 81B^2}$ $B = \frac{1}{\Omega} - 1$
Parabolic concentration profile $c_i(r,t) = c^m - 2\frac{c^\infty - c^m}{L}(r - R(t)) + \frac{c^\infty - c^m}{L^2}(r - R(t))^2$	$L_{par}(\Omega) = (\frac{1}{3}\sqrt[3]{5}(A_{par})^{\frac{1}{3}} - \frac{\sqrt[3]{25}}{3(A_{par})^{\frac{1}{3}}} - \frac{5}{3})R$ $A_{par} = 20 + 27B + 3\sqrt{3}\sqrt{15 + 40B + 27B^2}$ $B = \frac{1}{\Omega} - 1$
non-linear concentration profile $c_i(r,t) = (c^m - c^\infty)\frac{R}{r}(1 - \frac{r-R}{L}) + c^\infty$	$L_{mod}(\Omega) = (\frac{3}{2}(-1 + \sqrt{1 + \frac{8}{9}(\frac{1-\Omega}{\Omega})}))R$

Table 2.1: Functions of $L(\Omega)$ for different concentration profiles where $\Omega = \frac{c^\infty - c^m}{c^p - c^m}$.

To plot the concentration profiles of the neighboring particles, we need to adjust the initial concentration profiles as described below:

Linear approximation: $c_a(r,t) = c_i(-(r - (\langle d \rangle - L)), t) + (c_0^\infty - c^m)$
Parabolic approximation: $c_a(r,t) = c_i((r + (2L - (\langle d \rangle - 2R)), t)$
Non-linear approximation: $c_a(r,t) = c_i(-(r - \langle d \rangle), t)$

Here, $c_a(r,t)$ is the concentration profile of the neighboring particle for values of r in the range $(2x - R - L) < r < (2x - R)$.

2.4. Start of Soft Impingement (R_c)

First we calculate the critical radius the precipitate where soft impingement's starts (R_c). This is the radius of the particle where the concentration profile of the initial particle and neighboring particle meet. This is illustrated for the linear concentration profile in Figure 2.2.

Here, x is half of the average distance between the center of neighboring particles, we assume that all particles are at a distance $\langle d \rangle$ from each other. Since we know L for all three concentration profiles, we can calculate R_c.

$$R_c + L = x \tag{2.2}$$

For all concentration profiles, L can be written as

$$L = m(\Omega)R_c \tag{2.3}$$

This gives

$$R_c + m(\Omega)R_c = x \tag{2.4}$$

$$R_c(1 + m(\Omega)) = x \tag{2.5}$$

$$R_c = \frac{x}{1 + m(\Omega)} \tag{2.6}$$

Functions for $m(\Omega)$ are shown it Table 2.2. Since $m(\Omega)$ is different for each concentration profile, there will be different starting points for soft impingement.

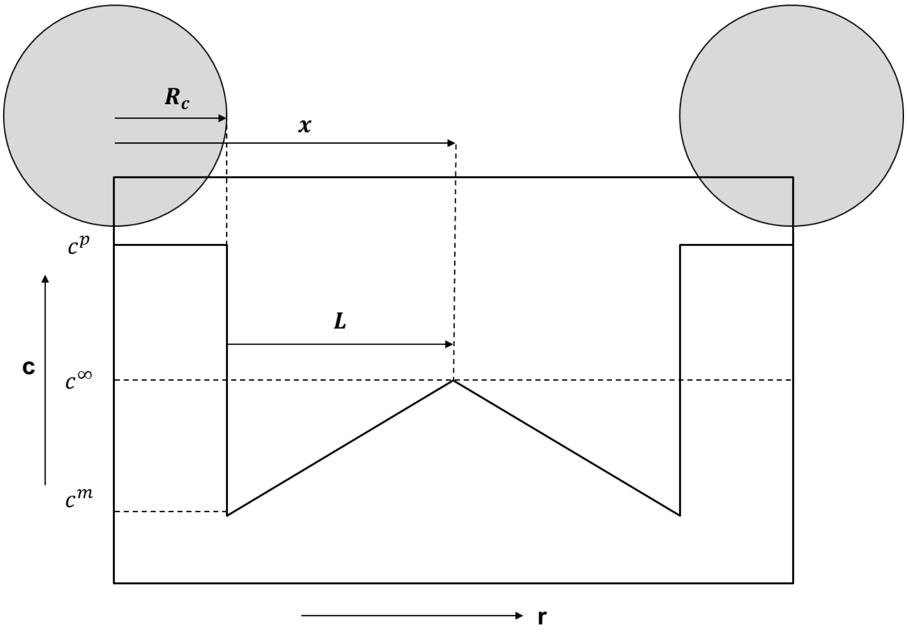

Figure 2.2: Start of soft impingement for the linear concentration profile approximation. R_c is the critical radius, L is the diffusion length, x is the distance from the center of the initial particle to the middle of the initial and neighboring particle.

Linear concentration profile $c(r,t) = \frac{c^\infty - c^m}{L}(r - R(t)) + c^m$	$m_{lin}(\Omega) = \frac{1}{3}(A_{lin})^{\frac{1}{3}} - \frac{2}{3(A_{lin})^{\frac{1}{3}}} - \frac{4}{3}$ $A_{lin} = 44 + 54B + 6\sqrt{54 + 132B + 81B^2}$ $B = \frac{1}{\Omega} - 1$
Parabolic concentration profile $c(r,t) = c^m - 2\frac{c^\infty - c^m}{L}(r - R(t)) + \frac{c^\infty - c^m}{L^2}(r - R(t))^2$	$m_{par}(\Omega) = \frac{1}{3}\sqrt[3]{5}(A_{par})^{\frac{1}{3}} - \frac{\sqrt[3]{25}}{3(A_{par})^{\frac{1}{3}}} - \frac{5}{3}$ $A_{par} = 20 + 27B + 3\sqrt{3}\sqrt{15 + 40B + 27B^2}$ $B = \frac{1}{\Omega} - 1$
Non-linear concentration profile $c(r,t) = (c^m - c^\infty)\frac{R}{r}(1 - \frac{r-R}{L}) + c^\infty$	$m_{mod}(\Omega) = (\frac{3}{2}(-1 + \sqrt{1 + \frac{8}{9}(\frac{1-\Omega}{\Omega})}))$

Table 2.2: Functions of $m(\Omega)$ for different concentration profiles where $\Omega = \frac{c^\infty - c^m}{c^p - c^m}$.

2.5. End of Growth (R_f)

The growth of the particle end when the concentration in the matrix reaches c^m, this happens when the particle radius reaches R_f and is independent of concentration profile approximation. This is illustrated in Figure 2.3.

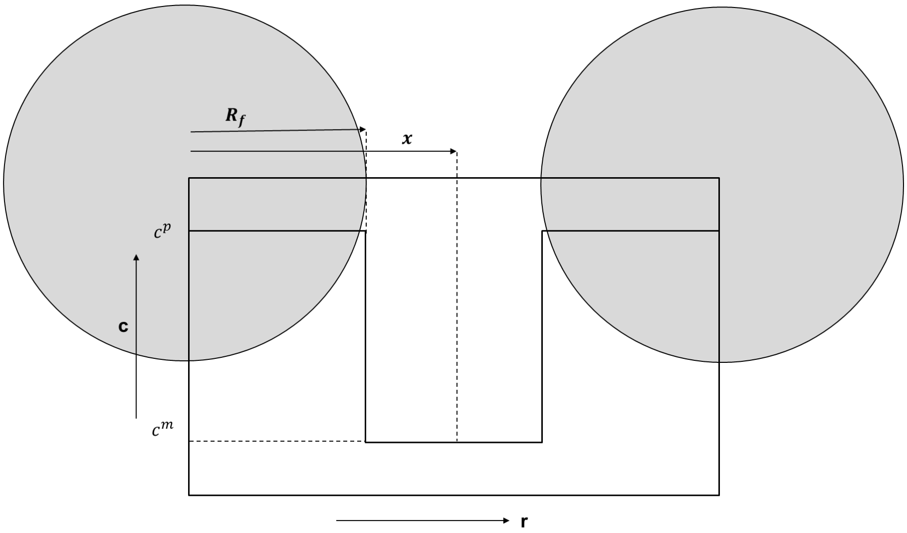

Figure 2.3: End of soft impingement and growth for any concentration profile approximation. R_c is the critical radius, L is the diffusion length, x is the distance from the center of the initial particle to the middle of the initial and neighboring particle.

To calculate R_f, we use the following mass balance

$$\int_0^{R_f} c^p 4\pi r^2 dr + \int_{R_f}^{x} c^m 4\pi r^2 dr = \int_0^{x} c^\infty 4\pi r^2 dr \tag{2.7}$$

Solving for R_f gives

$$R_f = x\Omega^{\frac{1}{3}} \tag{2.8}$$

Since R_f depends on the supersaturation and is independent of the concentration profile, it will be the same for all approximation.

2.6. Growth during Soft Impingement (c_s)

It is now known when soft impingement starts and ends. From Figure 2.2 and 2.3 it can be seen that the concentration at $r = x$ starts at c^∞ and ends at c^m. The concentration at $r = x$ during soft impingement will be in the following range: $c_0^\infty < c_s < c^m$. To define a function for c_s, we will use the following mass balance:

$$\int_0^{R} c^p 4\pi r^2 dr + \int_{R}^{x} c(r,t) 4\pi r^2 dr = \int_0^{x} c_0^\infty 4\pi r^2 dr \tag{2.9}$$

We replace c^∞ in the concentration profile by c_s since this changes over time. Also, since the function for L loses its meaning after soft impingement, we replace L by $x - R$. The full calculations for c_s for all concentration profile approximations are available in the appendix in **Appendix**. The concentration profiles and solutions of equation (2.9) are as followed:

Linear concentration profile

$$c(r,t) = \frac{c_s^{lin} - c^m}{x - R}(r - R) + c^m \tag{2.10}$$

$$c_s^{lin} = \frac{x^3(c_0^\infty - c^m) + R^3(c^m - c^p)}{A_1} + c^m \tag{2.11}$$

$$A_1 = 3\left(\frac{1}{x-R}\frac{1}{4}(x^4 - R^4) - \frac{R}{x-R}\frac{1}{3}(x^3 - R^3)\right) \tag{2.12}$$

Parabolic concentration profile

$$c(r,t) = c^m - 2\frac{c_s^{par} - c^m}{x - R}(r - R) + \frac{c_s^{par} - c^m}{(x-R)^2}(r - R)^2 \tag{2.13}$$

$$c_s^{par} = \frac{x^3(c_0^\infty - c^m) + R^3(c^m - c^p)}{A_2} + c^m \tag{2.14}$$

$$A_2 = 3(\frac{2}{x-R}(\frac{1}{4}(x^4 - R^4) - \frac{1}{3}R(x^3 - R^3)) - \frac{1}{(x-R)^2}(\frac{1}{5}(x^5 - R^5) - \frac{1}{2}R(x^4 - R^4) + \frac{1}{3}R^3(x^3 - R^3))) \tag{2.15}$$

Non-linear concentration profile

$$c(r,t) = (c^m - c_s^{mod})\frac{R}{r}(1 - \frac{r-R}{x-R}) + c_s^{mod} \tag{2.16}$$

$$c_s^{mod} = \frac{c_0^\infty x^3 - c^p R^3 - c^m A_3}{x^3 - R^3 - A_3} \tag{2.17}$$

$$A_3 = 3(\frac{1}{2}(x^2 - R^2)R - \frac{1}{x-R}(\frac{1}{3}(x^3 - R^3)R - \frac{1}{2}(x^2 - R^2)R^2)) \tag{2.18}$$

c_s will now replace c^∞ in the calculation of Ω.

$$\Omega = \frac{c_s - c^m}{c^p - c^m} \tag{2.19}$$

Note that c_s for all concentration profiles is a function of R, while we know that $R = f(\Omega)$. Therefore, the problem can only be solved numerically. For the model, we use c_s from the last time step to calculate R for the new time step.

2.7. Model Summary

In this part, we will explain the model shown in Figure 2.4. This chart is the basis for this thesis work.

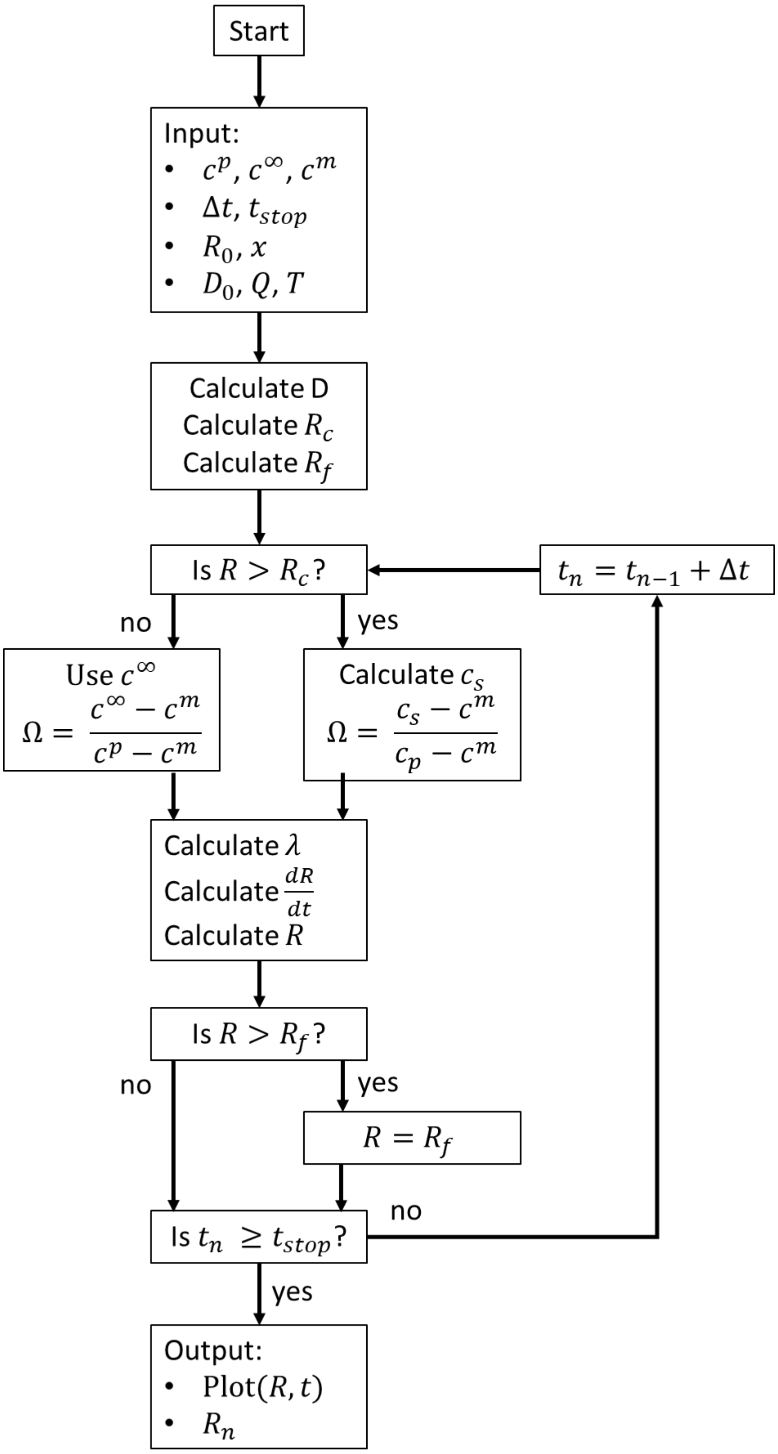
Start
Input:
• c^p, c^∞, c^m
• $\Delta t, t_{stop}$
• R_0, x
• D_0, Q, T
Calculate D
Calculate R_c
Calculate R_f
Is $R > R_c$?
$t_n = t_{n-1} + \Delta t$
no
yes
Use c^∞
$\Omega = \frac{c^\infty - c^m}{c^p - c^m}$
Calculate c_s
$\Omega = \frac{c_s - c^m}{c_p - c^m}$
Calculate λ
Calculate $\frac{dR}{dt}$
Calculate R
Is $R > R_f$?
no
yes
$R = R_f$
no
Is $t_n \geq t_{stop}$?
yes
Output:
• Plot(R, t)
• R_n

Figure 2.4: Soft impingement model chart of particle growth assuming diffusional growth.

To start, we need to input the concentration in the particle (c^p), in the matrix far from the particle (c^∞) and the concentration in the matrix at the particle interface (c^m). We also need a time step size (Δt) and an end time (t_{stop}). The end time is usually the time between nucleation and annealing time. Next, we need a starting size (R_0), this is the size of the particle after nucleation, and the average distance of the center of the particle until the middle of the initial and neighboring particle (x). Since we assume diffusional growth, we need the diffusion coefficient (D). We calculate D with

$$D = D_0 \exp\left(\frac{-Q}{R_{gc}T}\right) \tag{2.20}$$

Where D_0 is the pre-exponential factor, Q is the activation energy for diffusion ,T is the temperature (in K) and R_{gc} is the gas constant, not to be confused with the particle radius. With this, we first calculate R_c and R_f according to equation (2.6) and (2.8) respectively.

The iterative loops start here. At the start of the loop, we check if $R > R_c$. If this is not the case, soft impingement has not started and we will use c^∞ in the calculation of Ω. Else, the concentration profiles overlap, and we use c_s, according to equation (2.11), (2.14) or (2.17) depending on the concentration profile approximation, for the calculation of Ω. We use Ω and R to calculate λ according to equation (2.11), (2.14) or 2.17. $\frac{dR}{dt}$ is calculated by using the derivative of equation (1.1), given by

$$\frac{dR}{dt} = \frac{1}{2}\lambda\sqrt{\frac{D}{t}} \tag{2.21}$$

For R we use the following numerical calculation.

$$R_n = R_{n-1} + \left(\frac{dR}{dt}\right)_{t=t_{n-1}+\frac{1}{2}\Delta t} \cdot \Delta t \tag{2.22}$$

Due to the numerical nature of the model and the possibility of a large Δt, it is possible to pass R_f. In this case, the model will break. Therefore, if $R > R_f$, we set R back to the value calculated for R_f. This loop will continue until the final time is reached. From here it is possible to plot R as a function of time or give the final particle size R_n.

3

Additional Effects

In addition to the effect of soft impingement, we will add the effects of capillary forces (Gibbs Thomson Effect) from Perez et al. [15] and dislocation assisted growth, using the multi dislocation model from Porter et al. [16], the single dislocation model from Wang et al. [17], the multi boundary model [18] and the single boundary from Cheng et al. [19]. Lastly, we will summarize the soft impingement model with all its additions, including an updated flow chart. A more detailed description of the additional effects and calculations can be found in the appendix in **Chapter 6**.

3.1. Gibbs Thomson Effect

The Gibbs Thomson effect accounts for the effect interfacial energies have on the equilibrium concentration in the matrix at the interface of the particle (c^m). Most soft impingement models do not include the Gibbs Thomson effect, due to it only playing a role if we assume a spherical particle in 3D space. We will be using the same approximation for the Gibbs Thomson effect that Öhlund et al. [2] used. The approximation is from Perez et al. [15].

The general Gibbs-Thomson equation is given by

$$\frac{2\gamma v^{\beta}_{at}}{rkT} = (1 - c^p)ln(\frac{1 - c^m_R}{1 - c^m}) + c^p ln(\frac{c^m_R}{c^m}) \tag{3.1}$$

Where c^p, c^m and c^m_R are the solute concentration in the particle, in the matrix at the side of the interface without and with interfacial energies and v^{β}_{at} is the atomic volume of the particle. This equation does not have simple solutions. Perez [15] discussed three approximations for this equation, but we will only focus on one of the approximation since the other two are not applicable in the radii range of precipitation ($\sim 1.E - 09m$) according to Perez [15] as seen in Figure 3.1.
For the assumption where $c^m_R << 1$ and $c^m << 1$, the first term in equation (A.84) can be neglected and then rewritten so we obtain a function for c^m_R as

$$c^m_R = c^m exp(\frac{2\gamma v^{\beta}_{at}}{c^p RkT}) \tag{3.2}$$

We now have a function of c^m_R depending on R. Thus, this can only be solved numerically, similar to the functions of c_s. We will calculate c^m_R the same way that we calculate c_s, where at every loop we use R from the previous step. Now Ω depends on c^m_R and c_s as functions of R.

3.2. Assisted Growth Models

According to the classical nucleation theory, defects such as dislocations or boundaries serve as preferential nucleation sites for precipitates because relieving some of the stress and interfacial energy associated with defects lowers the activation energy for nucleation [20]. Wang et al.[17] mentioned the mechanisms in which dislocation affects growth. Dislocations can attract solute elements because of attractive forces from their stress fields. In addition, the diffusion coefficient inside the dislocations is higher than that of the matrix [7][16]. Dislocations will act as highly diffusive paths for the solute elements, increasing the growth rate of precipitates

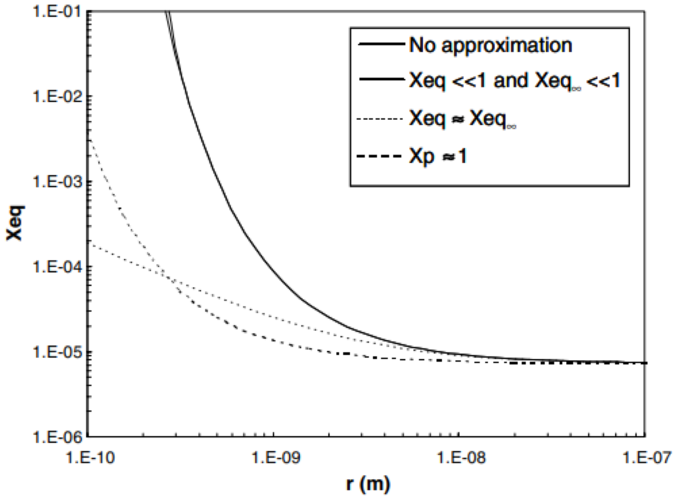

Figure 3.1: The exact solution of equation (A.84) compared with three approximations for Fe_3C precipitation [15]. Note that in this thesis, we use the following notation: $r = R$, $Xeq = c_R^m$ and $Xeq_\infty = c^m$, where c is the solute fraction.

located at the dislocation. Cheng et al. [19] mentioned a similar view on boundary diffusion. where boundaries will also act as highly diffusive paths. In this part, we will discuss four models to add to our model from **Chapter 2**, which include either the dislocation- or the boundary assisted growth effect.

3.2.1. Single Dislocation Model

Wang et al. [17] proposed a model to account for the effect that dislocations have on the growth rate of the precipitate. Their model is illustrated in Figure 3.2.

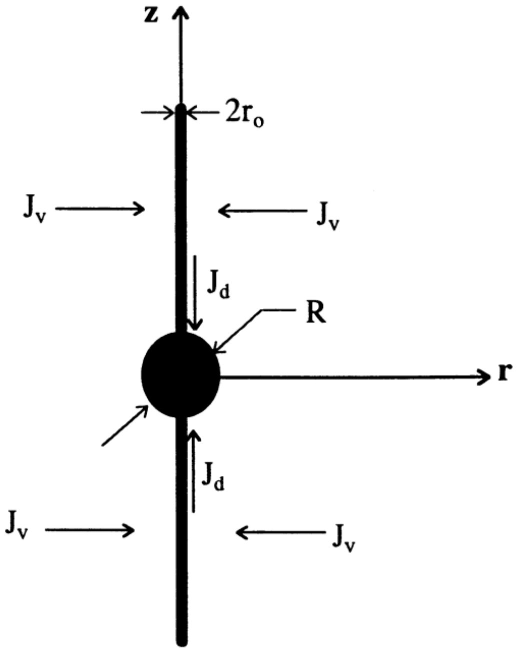

Figure 3.2: Simplified geometry of a particle on a dislocation line [17].

They assumed the precipitate to be a spherical particle, in this case, laying in the center of the dislocation line, which is assumed to be a cylinder with radius r_0, usually related to the burgers vector (**b**) [2][17]. The overall growth rate is approximated to be the sum of the growth rate due to the diffusion in the pipe and in the lattice.

$$\frac{dR}{dt}|_{th} = \frac{dR}{dt}|_l + \frac{dR}{dt}|_p \tag{3.3}$$

According to the model, $\frac{dR}{dt}|_p$ is given as

$$\frac{dR}{dt}|_p = \frac{c^\infty - c^m}{c^p - c^m}\frac{\sqrt{2}r_0}{\pi R^2}\sqrt{D_p D_l}\sqrt{f(t')} \tag{3.4}$$

Where

$$f(t') = \int_0^\infty \frac{exp(-t'x^2)}{x(J_0^2(x) + Y_0^2(x))}dx \tag{3.5}$$

and

$$t' = \frac{D_l t}{r_0^2} \tag{3.6}$$

Here, $J_0(x)$ and $Y_0(x)$ are Bessel functions of the first and second kind of the zeroth order and D_p is the diffusion coefficient of the solute in the dislocation pipe. To use the single dislocation model, we will add $\frac{dR}{dt}|_p$ to our previously calculated $\frac{dR}{dt}|_l$ and use this summation as the total growth rate.

3.2.2. Single Boundary Model

Cheng et al. [19] proposed a model similar to the single dislocation model, but focused on boundary diffusion. Their model is illustrated in Figure 3.3.

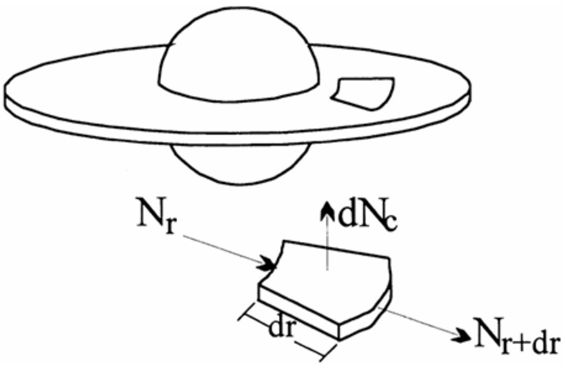

Figure 3.3: Simplified geometry of a particle on a boundary represented by a disk [19].

Here, they assumed a spherical precipitate located in the center of a disk with a finite thickness. The disk represents the boundary, and the mass diffusion is accelerated in the disk. Like the single dislocation model, the overall growth rate is approximated to be

$$\frac{dR}{dt}|_{th} = \frac{dR}{dt}|_l + \frac{dR}{dt}|_b \tag{3.7}$$

According to the model, $\frac{dR}{dt}|_b$ is given as

$$\frac{dR}{dt}|_b = \Omega(\frac{\delta D_b}{4R^2} + \frac{\delta D_b \beta}{2R} + (\frac{D_b}{\pi t})^{\frac{1}{2}}) \tag{3.8}$$

Where

$$\beta = \sqrt{\frac{4D_l}{D_b \delta d_0}} \tag{3.9}$$

Here, D_b is the diffusion coefficient in the boundary, δ is the boundary thickness and d_0 is the average grain size. This model does not include Bessel functions, as approximations were made to simplify them, as seen in the **Appendix**. In addition, Cheng et al. used the invariant size approximation [9] for $\frac{dR}{dl}|_l$. Here we will only use the function of $\frac{dR}{dl}|_b$ from the model and use the concentration profile approximations for $\frac{dR}{dl}|_l$. To include the single boundary model, we use the same process as for the single dislocation model.

3.2.3. Use of apparent diffusivities to describe high-diffusivity paths

The assisted growth effect of highly diffusive paths can also be described by an apparent diffusion coefficient. We will first introduce the multi dislocation model from from the book 'Phase Transformations in Metals and Alloys' by Porter and Easterling [16] and was used by Öhlund [2]. Secondly we will introduce a boundary assisted growth model which we will name 'the multi boundary model' mentioned in the book 'Microstructure Control in Metals' by Santofimia and Sietsma [18].

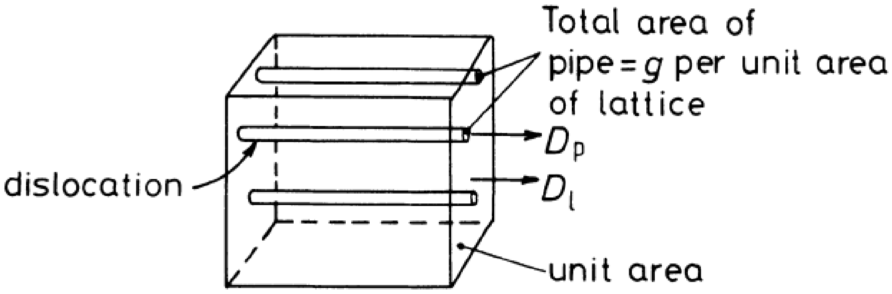

Figure 3.4: Multi dislocation model [16].

The multi dislocation model is illustrated in Figure 3.4. They assumed steady-state diffusion with equal concentration gradients through both the dislocation and the lattice. The atom fluxes are then equal to

$$J_l = -D_l \frac{dc}{dx} \tag{3.10}$$

$$J_p = -D_p \frac{dc}{dx} \tag{3.11}$$

Where D_l and D_p are the diffusion coefficient for the lattice and the dislocation or pipe respectively. The total flux then depends on the relative cross-sectional areas. Let us assume that the lattice area is A_l and the area of all dislocations in this area is A_p. Then the total flux is given as

$$J = \frac{J_l A_l + J_p A_p}{A_l} = -(\frac{D_l A_l + D_p A_p}{A_l})\frac{dc}{dx} \tag{3.12}$$

The apparent diffusion coefficient is then given as

$$D_{app} = \frac{D_l A_l + D_p A_p}{A_l} = D_l + D_p \frac{A_p}{A_l} \tag{3.13}$$

or

$$\frac{D_{app}}{D_l} = 1 + g\frac{D_p}{D_l} \tag{3.14}$$

Where g is the cross-sectional area of the dislocation per unit area of the lattice. Note that $g\frac{D_p}{D_l}$ is small at a larger temperature, due to rapid diffusion through the lattice. At lower temperatures, $g\frac{D_p}{D_l}$ is much larger, due to the lower activation energy for diffusion through the dislocation. According to Öhlund [2], g can be related to the dislocation density.

$$g = \rho\pi\mathbf{b}^2 \tag{3.15}$$

Where $\mathbf{b}$ is the burgers vector and ρ is the dislocation density. It is known that during annealing recovery of dislocations occurs which makes g a function of time. Öhlund extended equation (3.15) to include this recovery.

$$g(t) = \rho_{AsQ}\pi\mathbf{b}^2 - F(t)(\rho_{AsQ}\pi\mathbf{b}^2 - \rho_R\pi\mathbf{b}^2) \tag{3.16}$$

Where ρ_{AsQ} and ρ_R are the dislocation densities as quenched and after recovery respectively. $F(t)$ is a function that can be modelled to match the experimental data for the dislocation densities. Knowing the evolution of the dislocation density allows for a more accurate description of the apparent diffusion coefficient (D_{app}), but separate measurements must be taken of the dislocation density before the growth rate for the precipitates can be calculated. In addition, values for D_p for alloying elements are usually not available. Öhlund assumed the ratio of the pipe diffusion coefficient of the alloying element and the lattice diffusion coefficient to be related to the ratio between the lattice diffusion coefficient of the alloying element and iron, and the ratio of the matrix element self-diffusion through the dislocation and through the lattice. In the case of steel, this is given as

$$\frac{D_p^{x/alloy}}{D_l^{x/alloy}} = \frac{D_l^{x/Fe}}{D_l^{Fe/Fe}} * \frac{D_p^{Fe/Fe}}{D_l^{Fe/Fe}} \tag{3.17}$$

Where $\frac{D_p^{x/alloy}}{D_l^{x/alloy}}$ is the ratio between the pipe and lattice diffusion coefficient of element x in the alloy lattice, $\frac{D_l^{x/Fe}}{D_l^{Fe/Fe}}$ is the ratio between the lattice diffusion coefficient of element x and iron in an iron lattice and $\frac{D_p^{Fe/Fe}}{D_l^{Fe/Fe}}$ is the ratio between the pipe and lattice diffusion coefficient of iron in an iron lattice. The term $\frac{D_p^{Fe}}{D_l^{Fe}}$ will be different at different temperatures. The values of the diffusion coefficient in the lattice and in the dislocations are measured by Shima et al. [21] for high purity iron. To use the multi dislocation model, we will change D in the model to D_{app}. If the change in dislocation density is included, then we will calculate D_{app} at every time step.

The multi boundary model is illustrated in figure 3.5 [18]. It has a similar definition as the multi dislocation model where steady-state diffusion with equal concentration gradients through both the boundary and lattice is assumed.

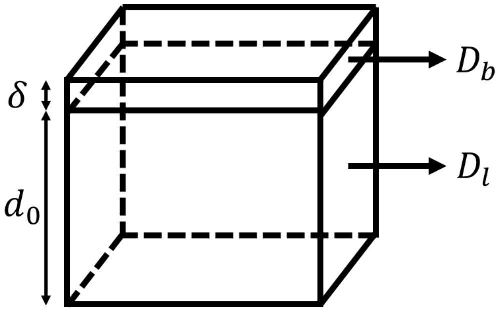

Figure 3.5: Multi boundary model.

The apparent diffusion coefficient can be written as

$$D_{app} = (1 - f_b)D_l + f_b D_b \tag{3.18}$$

Where D_b is the diffusion coefficient in the boundary and f_b is the volume fraction of the boundaries. f_b can be approximated as

$$f_b = \frac{\delta}{d_0} \tag{3.19}$$

Where δ and d_0 are the boundary thickness and mean grain diameter respectively. This gives

$$D_{app} = (1 - \frac{\delta}{d_0})D_l + \frac{\delta}{d_0}D_b \tag{3.20}$$

Since $f_b << 1$, we can approximate D_{app} to be

$$D_{app} = D_l + \frac{\delta}{d_0}D_b \tag{3.21}$$

3.3. Model Summary Including Additional Effects

In Figure 3.6, the model chart from the previous chapter can be seen with additional effects. This chart gives a summary of the models and indicates where in the soft impingement model is has an effect. The multi dislocation model and multi boundary model have an effect on the diffusion coefficient used at the start of the loop. Note that, for the multi dislocation model, if the dislocation density changes over time, the diffusion coefficient has to be recalculated after every time step. The Gibbs Thomson effect is used in the loop for the calculation of Ω. Lastly, the single dislocation model and the single boundary model are used in the loop to calculate the growth rate ($\frac{dR}{dt}|_t$). It is important to mention that the four assisted growth models can not be used at the same time. Only the Gibbs Thomson effect can be included and excluded in combination with any of the other models.

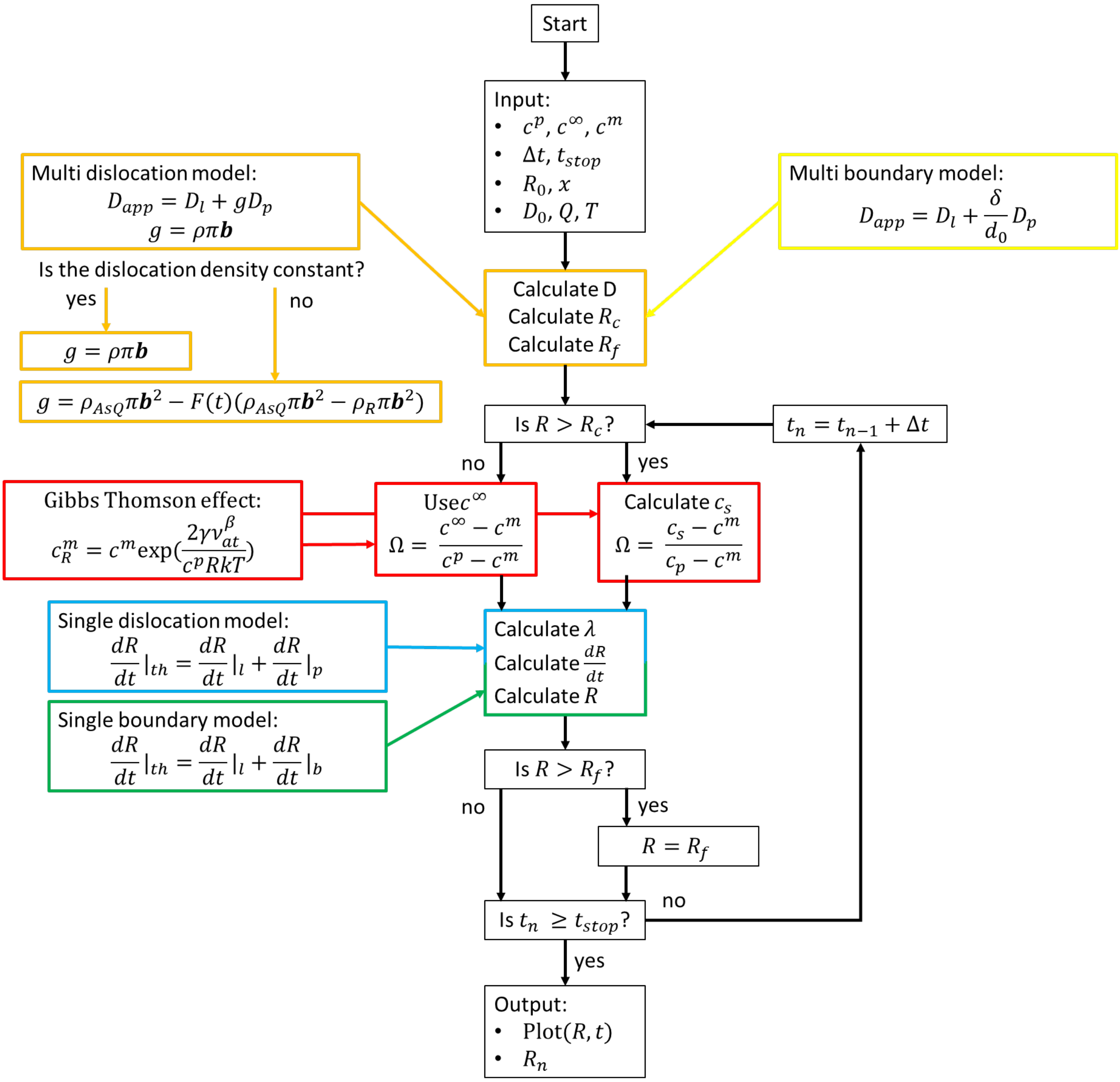
Start
Input:
c^p, c^∞, c^m
$\Delta t, t_{stop}$
R_0, x
D_0, Q, T
Multi dislocation model:
$D_{app} = D_l + gD_p$
$g = \rho\pi\boldsymbol{b}$
Is the dislocation density constant?
yes
no
$g = \rho\pi\boldsymbol{b}$
$g = \rho_{AsQ}\pi\boldsymbol{b}^2 - F(t)(\rho_{AsQ}\pi\boldsymbol{b}^2 - \rho_R\pi\boldsymbol{b}^2)$
Multi boundary model:
$D_{app} = D_l + \frac{\delta}{d_0}D_p$
Calculate D
Calculate R_c
Calculate R_f
Is $R > R_c$?
$t_n = t_{n-1} + \Delta t$
no
yes
Gibbs Thomson effect:
$c_R^m = c^m \exp(\frac{2\gamma v_{at}^\beta}{c^p RkT})$
Usec^∞
$\Omega = \frac{c^\infty - c^m}{c^p - c^m}$
Calculate c_s
$\Omega = \frac{c_s - c^m}{c_p - c^m}$
Single dislocation model:
$\frac{dR}{dt}|_{th} = \frac{dR}{dt}|_l + \frac{dR}{dt}|_p$
Single boundary model:
$\frac{dR}{dt}|_{th} = \frac{dR}{dt}|_l + \frac{dR}{dt}|_b$
Calculate λ
Calculate $\frac{dR}{dt}$
Calculate R
Is $R > R_f$?
no
yes
$R = R_f$
no
Is $t_n \geq t_{stop}$?
yes
Output:
Plot(R, t)
R_n

Figure 3.6: Soft impingement model chart of particle growth assuming diffusional growth including additional effects. Orange is the multi dislocation model, blue is the single dislocation model, yellow is the multi boundary model. green is the single boundary model and red is the Gibbs Thomson effect. Note that out of the four assisted growth models only one can be used at a time. The Gibbs Thomson effect can be included or excluded in combination with any of the models.

4

Application and Discussion

Here, we will apply the model to data for TiC precipitation in martensitic steel. First we will introduce the input data, used for the soft impingement model and the additional effects. Then we will discuss and visualize the effects of using difference concentration profile approximations, the Gibbs Thomson effect and the assisted growth models. Lastly, we will compare the present model with experimental data and a theoretical model by Öhlund et al. [2]. We will focus on a Fe-Ti-Mn-C martensitic steel with the composition shown in Table 4.1.

C	Mn	Si	P	S	Al	Ti	Cu	Cr	O	V
0.39	0.8700	0.0040	0.0011	0.0007	0.0047	0.0420	0.0012	0.0022	0.0046	0.0022

Table 4.1: Input data for the soft impingement model.

Figure 4.1 shows the heat treatment on the steel. This visualizes the time range in which we will apply our model. First, the material is homogenized at 1350°C to fully dissolve TiC in solid solution. The material is then quenched at 180° C / s until the start temperature of martensite, which is around 380-390°C [2]. After that, it continues to cool at 45° C until room temperature. The material is heated up at 4°C/s until the tempering temperature of 550°C. Here, it is kept for 60 min. This is the stage that allows the TiC precipitates to nucleate and grow. According to Öhlund [2], the nucleation of the particles in the boundary (martensite laths) starts after 5 minutes of tempering and the nucleation in the matrix starts after 10-30 minutes of tempering. Our model will be applied in the time range between nucleation and the end of the tempering stage.

4.1. Input data

Table 4.2 shows the input data for the soft impingement model. The equilibrium concentration of Ti in the particle (c^p) and in the matrix at the interface of the particle (c^m) are from ThemoCalc [22]. c^∞ is from experimental data [2]. For Δt, one second is chosen. Increasing the time step would make the results less accurate, but decrease the simulation time. The increase in accuracy for time steps smaller than one second seems to be negligible. t_{stop} is 3300 for nucleation on the boundary and 3000 or 1800 for nucleation in the matrix, according to Figure 4.1. Note that the only difference, whether we focus on matrix nucleation or boundary nucleation, is the nucleation time. Thus, precipitates in the matrix have 1800 - 3000 seconds to grow, while at the boundary the precipitates have 3300 seconds to grow. The starting size of the particle (R_0) is approximated to be 0.2 nm, which is the critical radius of a TiC nucleus [2]. The half distance between the centers of two precipitates (x) was estimated to be 5 nm according to the APT results (5 - 7.5 nm) [2].

c^p (wt%)	c^m (wt%)	c^∞ (wt%)	Ω	Δt (s)	t_{stop} (s)	R_0 (nm)	x (nm)
79.654	0.00084	0.042	0.0005	1	3300/3000/1800	0.2	5

Table 4.2: Input data for the soft impingement model [2]. Ω is rounded to 0.0005.

Table 4.3 shows the diffusion data for TiC used in equation (2.20) [2].

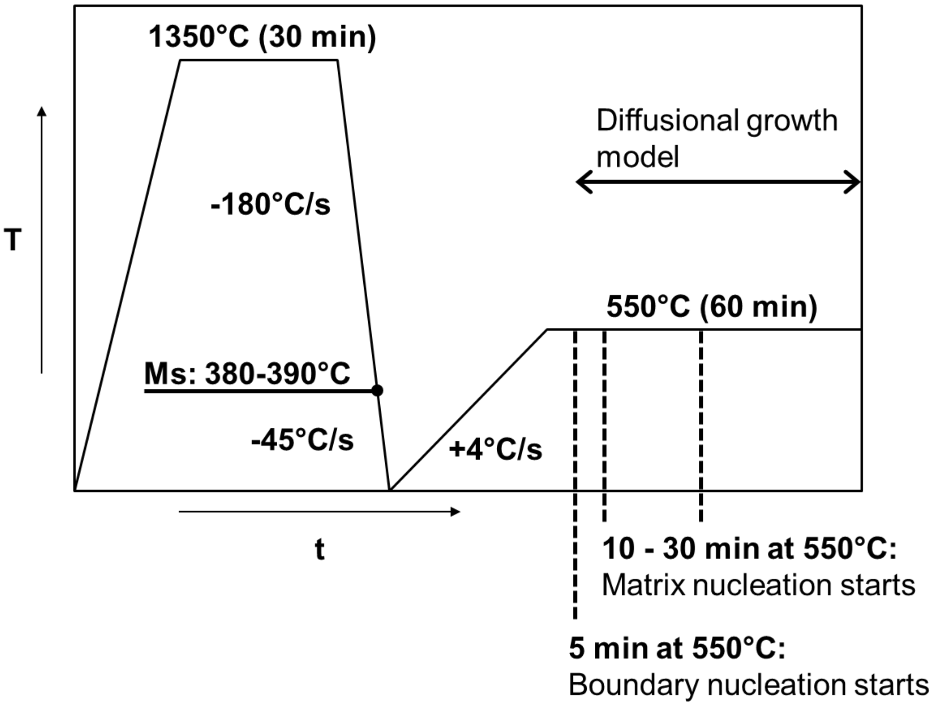
1350°C (30 min)
Diffusional growth model
-180°C/s
T
550°C (60 min)
Ms: 380-390°C
-45°C/s
+4°C/s
t
10 - 30 min at 550°C:
Matrix nucleation starts
5 min at 550°C:
Boundary nucleation starts

Figure 4.1: Heat treatment of Fe-Mn-Ti-C Steel according to Öhlund et al. [2].

D_0 (m^2/s)	Q (J/mol)	T (K)
0.21	307010	823.15

Table 4.3: Diffusion data [2].

4.2. Concentration profile effect excluding soft impingement

First, we will compare the different concentration profile approximations without soft impingement. This is done by ignoring the check if $R > R_c$. The aim is to compare the results with the exact solution. We can only use the exact solution if soft impingement is not involved, since it is not possible to get a function for c_s from the exact solution.

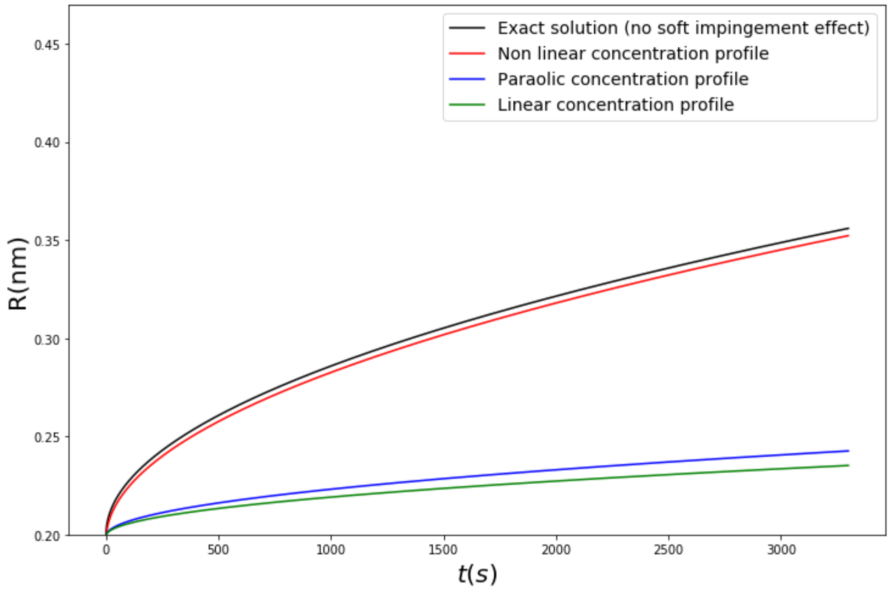

Figure 4.2: TiC precipitate growth according to the diffusional growth model excluding soft impingement.

Figure 4.2 shows the results from using the model with the input data from Table 4.2. Figure 4.2 shows the growth for 3300 seconds, but if we stop at 1800 - 3000 seconds, we will obtain the results for matrix diffusion.

Table 4.4 shows the size of the precipitate at the end of tempering and the maximum precipitate size (R_f) according to the mass balance. We will focus more on the limitation of R_f in the next chapters.

	R_{exact} (nm)	R_{linear} (nm)	$R_{parabolic}$ (nm)	$R_{non-linear}$ (nm)	R_f (nm)
Boundary nucleation	0.356	0.235	0.243	0.352	0.401
Matrix nucleation	0.315 - 0.349	0.226 - 0.234	0.231 - 0.241	0.312 - 0.345	0.401

Table 4.4: Precipitate size results excluding soft impingement. The results for boundary nucleation are gained at $t = 3300$ and for matrix nucleation at $t = 1800$ and $t = 3000$.

Figure 4.2 and Table 4.4 confirm our initial comparison for the different concentration profile approximations from Figures 1.6 and 1.7. The results show that the non-linear concentration profile approximation gives more accurate results than the linear and the parabolic concentration profile approximation. Figures 1.6 and 1.7 show that the difference is very large at small Ω. We can see this in the results, since $\Omega = 0.0005$. Figures 1.6 only show the difference in λ at a given value for Ω, but do not indicate where the difference in λ comes from. For this, we have to go back to the flux balance equation

$$(c^m - c^p)\frac{dR}{dt} = -D\frac{\delta c}{\delta r}\bigg|_R \tag{4.1}$$

Here, we can see that the growth rate ($\frac{dR}{dt}$) depends on the diffusion coefficient and the slope of the concentration profile at the precipitate interface. D is the same for all concentration profile approximations, but the slope will differ. Figure 4.3 shows the three concentration profile approximations and confirms the effect that the profiles have on the flux balance equation. The non-linear concentration profile has the steepest slope at the interface and thus the largest growth rate. The parabolic profile has a slightly steeper slope, thus a sightly larger growth rate than the linear profile, which aligns with the results in Figure 4.2.

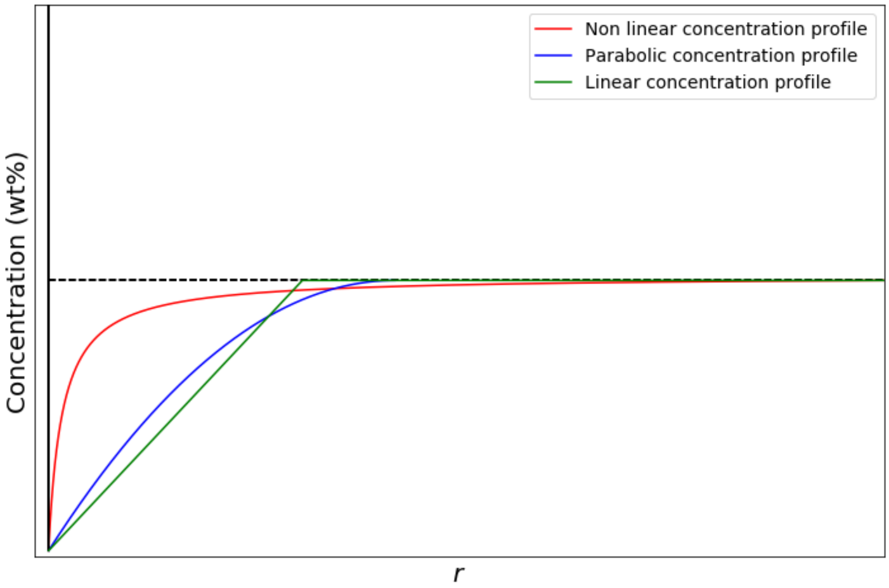

Figure 4.3: Solute concentration profiles in front of the interface of the precipitate at $R = R_c^{non-linear}$.

4.3. Concentration profile effect including soft impingement

In this part, we include the effect of soft impingement. In other words, c_∞ is replaced by c_s and changes over time from c_∞ to c^m. Here, R_c and R_f become important. Figure 4.4 visualizes the solute concentration profiles at the start of the growth (R_0). Table 4.5 shows the results for R_c for each concentration profile and R_f. R_c differs for each approximation since R_c depends on the diffusion length.

$R_c^{non-linear}$ and $R_c^{parabolic}$ are smaller than R_0. Because of this, the effect of soft impingement is already present at the start of growth for the non-linear and parabolic concentration profile approximation. During growth, if R_c has not been reached, the diffusion length will increase until the end of the concentration profile reaches $r = x$. At this point, soft impingement takes effect, decreasing c_s. In both steps, the slope at the interface of the particle is decreasing. This decreases the growth rate. In addition, a lower value for c_s will decrease the

R_c^{linear} (nm)	$R_c^{parabolic}$ (nm)	$R_c^{non-linear}$ (nm)	R_f (nm)	R_0 (nm)
0.257	0.191	0.081	0.401	0.2

Table 4.5: The critical radius (R_c) for all approximations, the maximum precipitate size according to the mass balance (R_f) and the critical nuclei size (R_0).

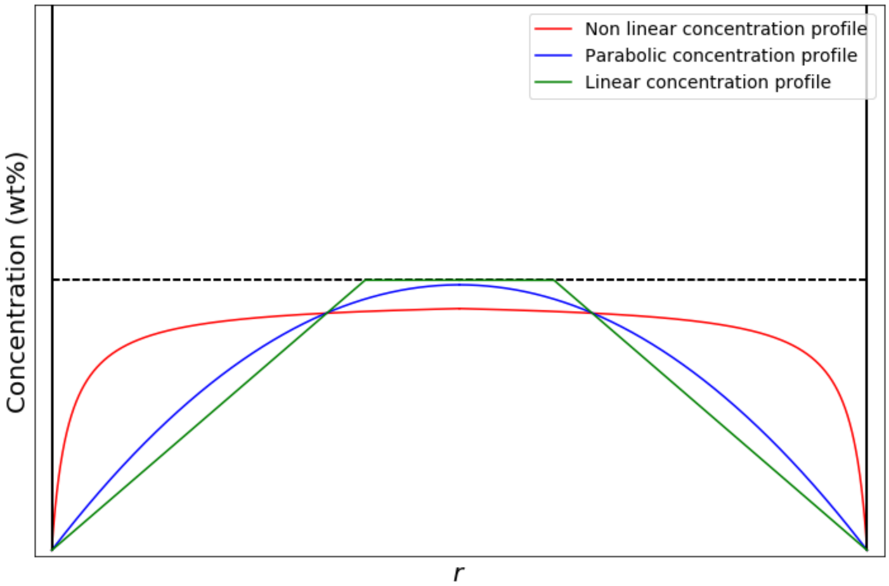

Figure 4.4: Solute concentration profiles between the initial and neighboring particle at $R = R_0$.

supersaturation and in turn decrease the growth rate.
Table 4.6 shows the size of the precipitate at the end of tempering, including and excluding soft impingement. It shows that there is no change in R_{linear} since R_0 has not been reached, soft impingement did not occur. $R_{parabolic}$ changes slightly and $R_{non-linear}$ changes more noticeably due to larger λ than the other approximations.

	R_{linear} (nm)	$R_{parabolic}$ (nm)	$R_{non-linear}$ (nm)
BN	0.235	0.243	0.352
BN + SI	0.235	0.241	0.328
MN	0.226 - 0.234	0.231 - 0.241	0.312 - 0.345
MN + SI	0.226 - 0.234	0.230 - 0.239	0.298 - 0.322

Table 4.6: Precipitate size results. BN = Boundary nucleation, MN = Matrix nucleation, SI = soft impingement. The results for boundary nucleation are gained at $t = 3300$ and for matrix nucleation at $t = 1800$ and $t = 3000$.

Figure 4.5 shows the results of the soft impingement model and the exact solution without the soft impingement effect. Compared to Figure 4.2, we can clearly see the effect of soft impingement on the non-linear concentration profile. The results do not change for the linear and barely change for the parabolic concentration profile approximation.

4.4. Application of the Gibbs Thomson effect

For the Gibbs Thomson effect, we assume γ to be 0.3 J/m^2 [2]. Figure 4.6 shows the lattice structure of a TiC crystal. Since one unit cell contains four Ti atoms, we assume that the atomic volume of a Ti atom is one fourth of the volume of the unit cell with lattice parameter $a = 0.433$ nm. Table 4.7 shows the size of the precipitate at the end of tempering including and excluding the Gibbs Thomson effect. From the results, we see that adding the Gibbs Thomson effect barely reduces the size of the precipitates.

Figure 4.7 shows the change in c_R^m for all concentration profile approximations over time and Figure 4.8 shows the change in c_R^m related to the precipitate size. In the latter, the non-linear concentration profile is shown, since this approximation gives the largest precipitate size. The linear and parabolic concentration profile approximation will have the same trend but will reach a higher value for c_R^m at the end, since the precipitate is smaller. Both Figure 4.7 and Figure 4.8 show that the Gibbs Thomson effect is present but small. At the start of growth, the effect is at its largest at a 7 % increase in solute concentration. c_R^m decrease as the particle grows bigger.

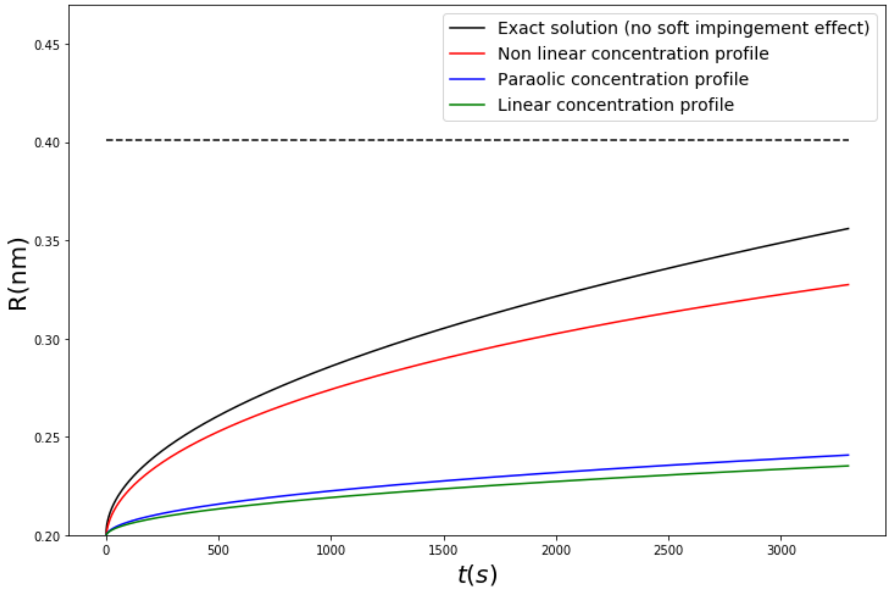

Figure 4.5: TiC precipitate growth according to the diffusional growth model including soft impingement. The exact solution does not include the soft impingement effect. The dotted line indicates $R_f = 0.401$ nm.

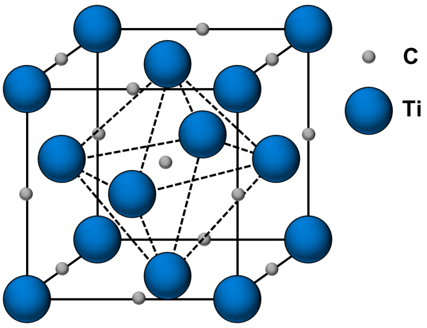

Figure 4.6: Lattice structure of a TiC crystal.

	R_{linear} (nm)	$R_{parabolic}$ (nm)	$R_{non-linear}$ (nm)
BN + SI	0.235	0.241	0.328
BN + SI + GT	0.235	0.241	0.327
MN + SI	0.226 - 0.234	0.230 - 0.239	0.298 - 0.322
MN + SI + GT	0.226 - 0.233	0.230 - 0.239	0.298 - 0.322

Table 4.7: Precipitate size results. BN = Boundary nucleation, MN = Matrix nucleation, SI = soft impingement, GT = Gibbs Thomson effect. The results for boundary nucleation are gained at $t = 3300$ and for matrix nucleation at $t = 1800$ and $t = 3000$.

In this case, the Gibbs Thomson slightly decreases the growth rate, but it has a negligible effect on the particle size for all concentration profile approximations. If it is reasonable to assume that there is no Gibbs Thomson effect depends mainly on R, γ and T according to equation (3.2). Especially small particles with a large surface tension at low temperatures will be affected. In our case, the Gibbs Thomson effect can be neglected.

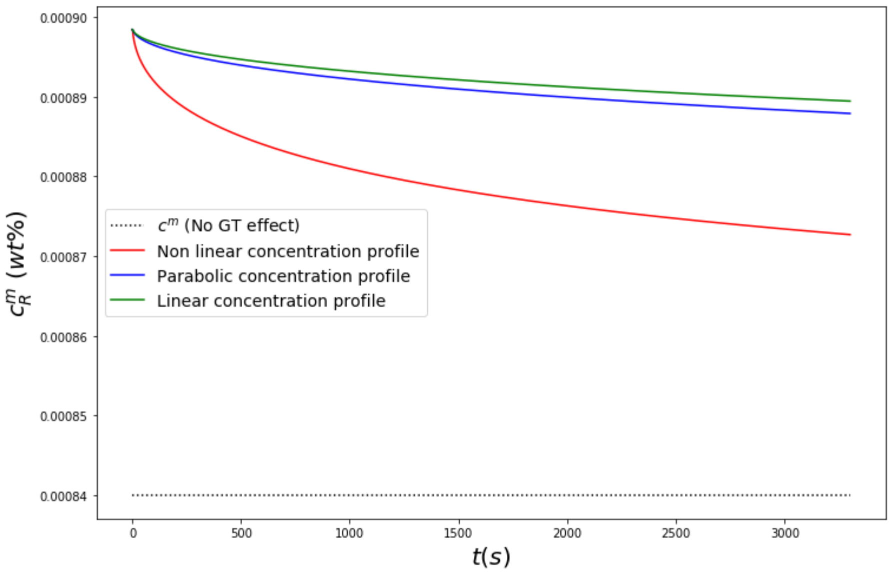

Figure 4.7: Change of c_R^m over time due to the Gibbs Thomson effect. The dotted line indicates $c^m = 0.00084\ wt\%$.

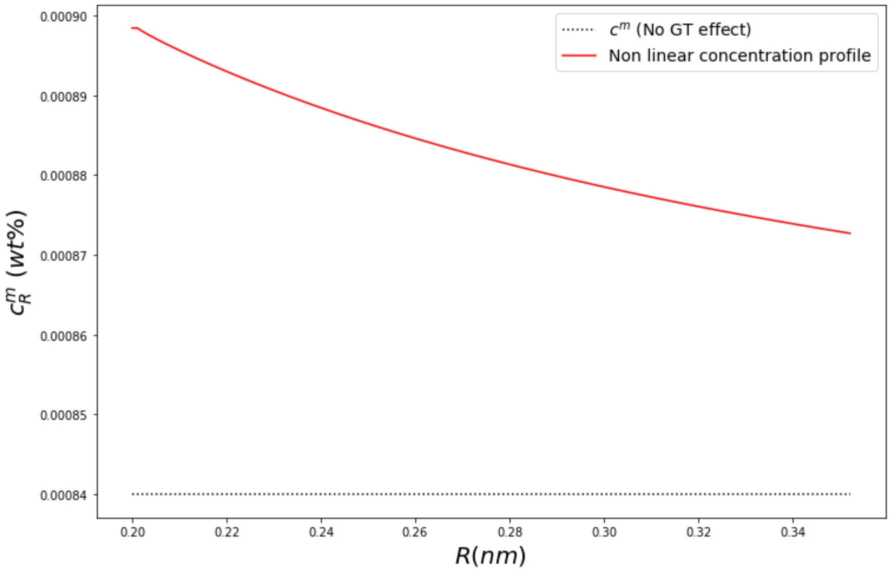

Figure 4.8: Change of c_R^m over R due to the Gibbs Thomson effect. The dotted line indicates $c^m = 0.00084\ wt\%$.

4.5. Application of the assisted growth models

For the results of the assisted growth models, we will neglect the Gibbs Thomson effect since it does not affect the results.

4.5.1. Multi dislocation model

With the use of the Multi dislocation model, we replace D with D_{app} according to equation (3.13). To our knowledge, D_p^{Ti} is not available. We will use the approximation from equation (3.17). The ratio $\frac{D_l^{Ti/Fe}}{D_l^{Fe/Fe}}$ and $\frac{D_p^{Fe/Fe}}{D_l^{Fe/Fe}}$ are 51700 and 0.3 at 550°C respectively [2]. This gives $\frac{D_p}{D_l} = 171300$. Since dislocation density data are available [2], we will use equation (3.16) for $g(t)$, where **b** is the Burgers vector. The dislocation density after quenching is given by $\rho_{AsQ} = 14.2 \times 10^{14} m^{-2}$ and the dislocation density after recovery (ρ_R) is set to $0.025 \times \rho_{AsQ}$. According to Öhlund et al. [2], the dislocation density is 55% of ρ_R after 5 minutes of annealing. Since the first nuclei, according to the model, start to form after 5 minutes, we assume a linear function for $F(t)$ from 0.55 to 1. Figure 4.9 shows the evolution of $F(t)$ from 5 min of annealing to 60 min of annealing. At t = 0, boundary nucleation starts and the dislocation density will change from 55% to 100% of ρ_R. The nucleation in the matrix starts at t = 300 - 1500. Since nucleation in the matrix starts later, the dislocation density at the start is lower compared to boundary nucleation.

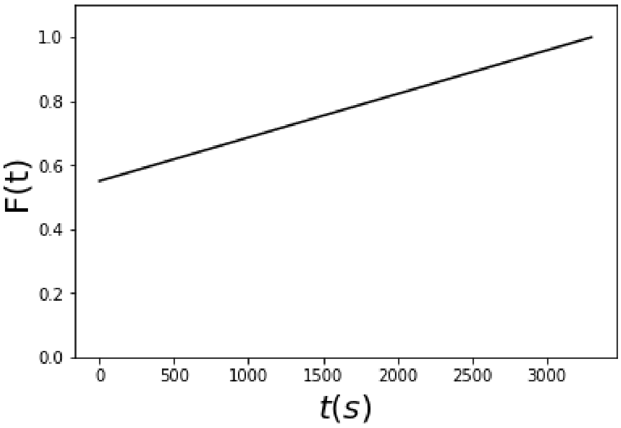

Figure 4.9: Evolution of F(t) over annealing time.

Table 4.8 shows the size of the precipitate at the end of tempering including and excluding the Multi dislocation model. All concentration profile approximations show increased particle size when the multi dislocation model is included. The non-linear concentration profile approximation reaches R_f before the end of annealing.

	R_{linear} (nm)	$R_{parabolic}$ (nm)	$R_{non-linear}$ (nm)
BN + SI	0.235	0.241	0.328
BN + SI + MD	0.326	0.335	0.401
MN + SI	0.226 - 0.234	0.230 - 0.239	0.298 - 0.322
MN + SI + MD	0.278 - 0.318	0.286 - 0.326	0.401

Table 4.8: Precipitate size results. BN = Boundary nucleation, MN = Matrix nucleation, SI = soft impingement, MD = Multi dislocation model. The results for boundary nucleation are gained at t = 3300 and for matrix nucleation at t = 1800 and t = 3000.

Figure 4.10 shows the results of the soft impingement model, including the multi dislocation model. Compared to Figure 4.5, it shows that the growth rate is faster for all concentration profile approximations. The non-linear concentration profile approximation even reaches R_f before the end of tempering, at $t = 723s$.

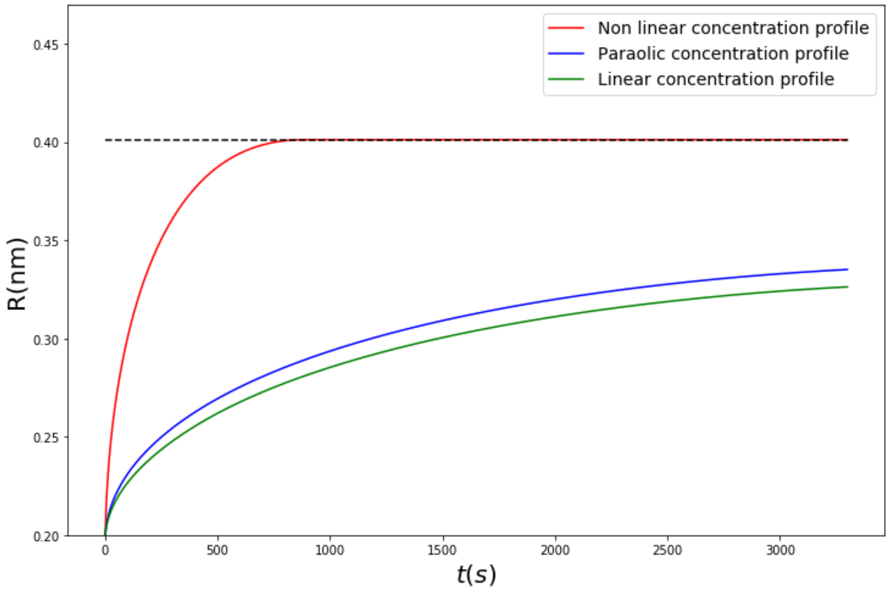

Figure 4.10: TiC precipitate growth according to the diffusional growth model including soft impingement and the multi dislocation model. The dotted line indicates R_f = 0.401 nm.

Figure 4.11 shows the change of D_{app} during particle growth. The decrease in the diffusion coefficient represents the decrease in dislocation density during annealing. The impact of this model is larger at the beginning of growth and decreases as the dislocation density decreases.

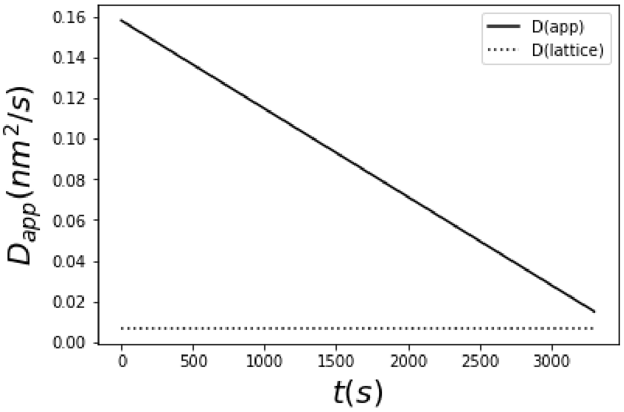

Figure 4.11: Evolution of D_{app} during particle growth. $D_{lattice} = 0.007\ nm^2/s$.

4.5.2. Single dislocation model

With the single dislocation model we use the overall growth rate according to equation (3.3). For the radius of the dislocation pipe (r_0) we assume the burgers vector. D_p^{Ti} is approximated the same as in the multi dislocation model. Table 4.9 shows the size of the precipitate at the end of tempering including and excluding the single dislocation model. We can see that for all concentration profile approximations, the precipitate reaches R_f before the end of tempering. The single dislocation model has a larger assisting growth affect than the multi dislocation model.

	R_{linear} (nm)	$R_{parabolic}$ (nm)	$R_{non-linear}$ (nm)
BN + SI	0.235	0.241	0.328
BN + SI + SD	0.401	0.401	0.401
MN + SI	0.226 - 0.234	0.230 - 0.239	0.298 - 0.322
MN + SI + SD	0.401	0.401	0.401

Table 4.9: Precipitate size results. BN = Boundary nucleation, MN = Matrix nucleation, SI = soft impingement, SD = Single dislocation model. The results for boundary nucleation are gained at $t = 3300$ and for matrix nucleation at $t = 1800$ and $t = 3000$.

Figure 4.12 shows the results of the soft impingement model, including the single dislocation model. From this, the greater assisting effect of this model is more apparent. It also seems that the concentration profile approximation has little effect on the growth when the single dislocation model is included.

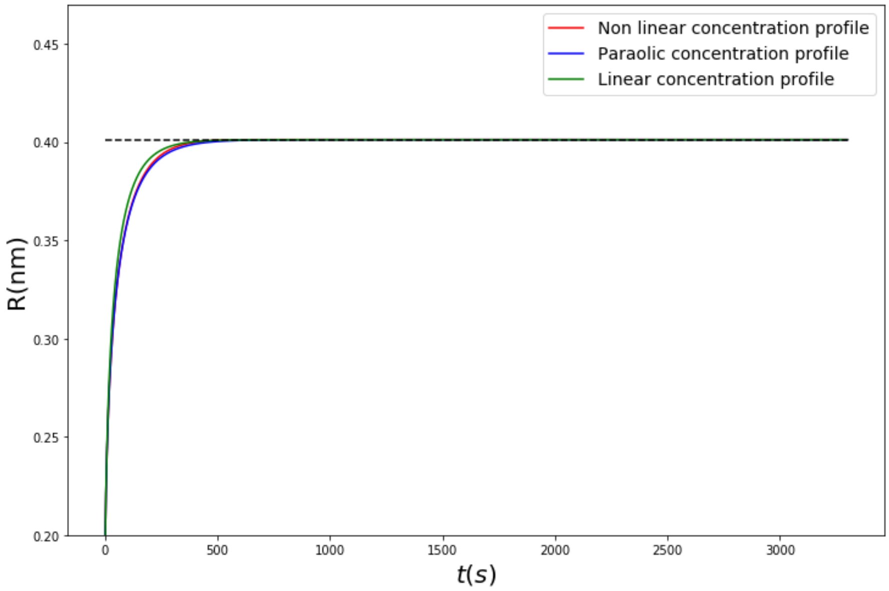

Figure 4.12: TiC precipitate growth according to the diffusional growth model including soft impingement and the single dislocation model. The dotted line indicates $R_f = 0.401$ nm.

	t_{linear} (s)	$t_{parabolic}$ (s)	$t_{non-linear}$ (s)
SI + SD	336	411	367

Table 4.10: Time of growth until R_f is reached for the different concentration profile approximations. SI = soft impingement, SD = Single dislocation model.

Table 4.10 shows the time for each concentration profile approximation, using the single dislocation model, to reach R_f. This gives results contradicting our previous results. We would expect the non-linear concentration profile approximation to have reached R_f first due to its largest parabolic growth constant (λ). The reason for this is due to the small radii range in which we are working. The particle size (R_f = 0.401 nm) is a size similar to the diameter of the dislocation pipe ($2 * r0$ = 0.498 nm). Therefore, according to the model, the growth rate due to diffusion in the pipe will be dominant in the whole growth stage. The only term in equation (3.4) for $\frac{dR}{dt}|_{pipe}$ depending on the concentration profile approximation is c^{∞} since we use the soft impingement model to replace c^{∞} with c_s after soft impingement. A higher value for c_s will yield a higher value for the value for $\frac{c_s - c^m}{c^p - c^m}$, which in turn yields a higher value for $\frac{dR}{dt}|_{pipe}$. From Figure 4.4, which indicates the concentration profile at the start of soft impingement, it is shown that the linear concentration profile has not started soft impingement and therefore will use c^{∞} in equation (3.4). For the non-linear concentration profile, we use c_s since soft impingement has already started and since this is lower than c^{∞}, $\frac{dR}{dt}|_{pipe}$ will be smaller than for the linear concentration profile. So far, this explains the contradiction in the results between the linear and non-linear concentration profile approximation, but not the parabolic. The reason why the parabolic concentration profile approximation is still in agreement with previous results is that the growth rate from the lattice ($\frac{dR}{dt}|_{lattice}$) is still much larger for the non-linear. Note that the total growth rate is the summation of both. The parabolic concentration profile approximation does indeed have a larger effect of the pipe diffusion, but is not large enough to compensate for its lack in volume diffusion. Figure 4.13 shows the growth rate from the lattice and the pipe for all concentration profile approximations for the first 100 seconds. Here, it is more apparent that the non-linear concentration profile approximation is indeed the one that has the lowest growth rate from the pipe but the largest growth rate from the lattice.

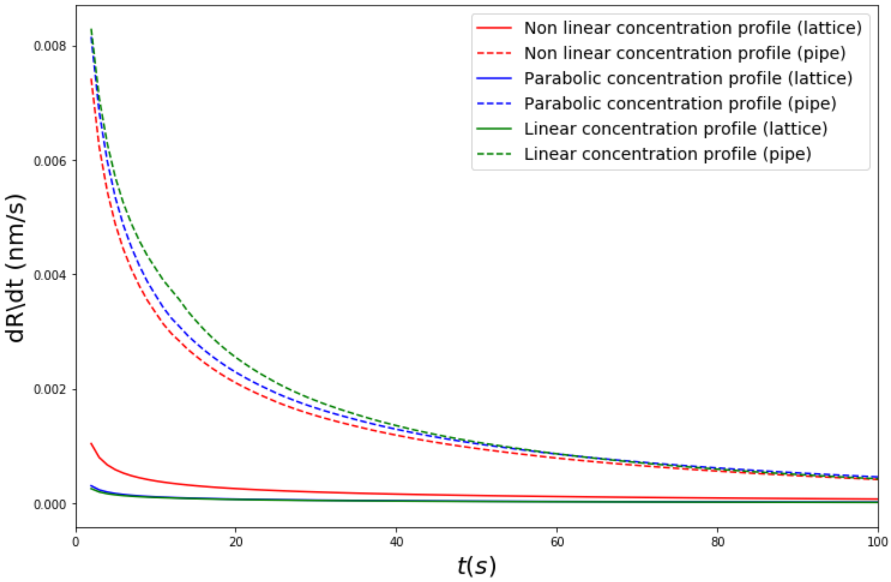

Figure 4.13: The lattice and pipe growth rate for all concentration profiles approximation from the single dislocation model for the first 100 seconds of growth.

Figure 4.14 shows the effect of different ratios for $\frac{D_p}{D_l}$ on precipitate growth using the non-linear concentration profile approximation. Growth increases with increasing diffusion coefficient in the pipe. It can also be seen that, if the diffusion coefficient in the pipe and in the lattice are identical, there is still an assisted growth effect. This is due to the summation of both growth rates, where the volume of the pipe is also counted when the volume diffusion is calculated.

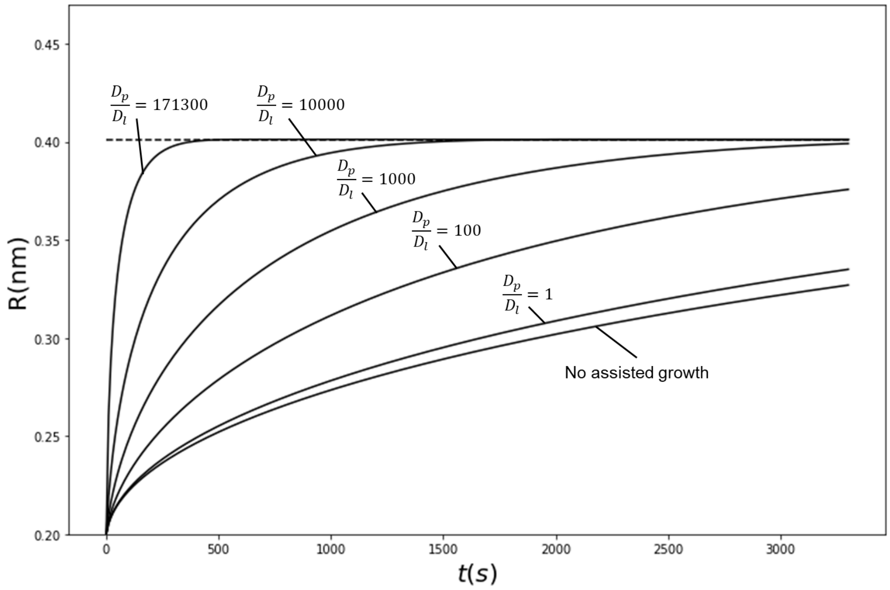

Figure 4.14: Effect of the pipe diffusion coefficient and lattice diffusion coefficient ration ($\frac{D_p}{D_l}$).

4.5.3. Multi boundary model

The implementation of the multi boundary model is the same as the multi dislocation model, but without the change of D_{app} over time. For the diffusion coefficient in the boundary (D_b), we assume that it is the same as the diffusion coefficient in the pipe (D_p). The boundary thickness (δ) is assumed to be the same as the diameter of the dislocation pipe, and the average grain size (d_0) is assumed to be 20 µm. Table 4.11 shows the the results for the soft impingement model, including the multi boundary model.

	R_{linear} (nm)	$R_{parabolic}$ (nm)	$R_{non-linear}$ (nm)
BN + SI	0.235	0.241	0.328
BN + SI + MB	0.280	0.288	0.401

Table 4.11: Precipitate size results. BN = Boundary nucleation, MN = Matrix nucleation, SI = soft impingement, MB = Multi boundary model. The results for boundary nucleation are gained at t = 3300.

The results show a similar trend as the volume diffusion model and the multi dislocation model. Figure 4.15 shows the results of the soft impingement model, including the multi boundary model. It can be seen that the assisted effect is present but small compared to volume diffusion. The non-linear concentration profile approximation reaches R_f in t = 2816 seconds.

In this case, D_{app} is constant at 0.036 nm^2/s while D_l = 0.007 nm^2/s. We can see the effect of this small increase in the results. The multi dislocation model has a much higher D_{app}, starting at D_{app} = 0.16 nm^2/s which causes the particle to reach larger sizes than for the multi boundary model.

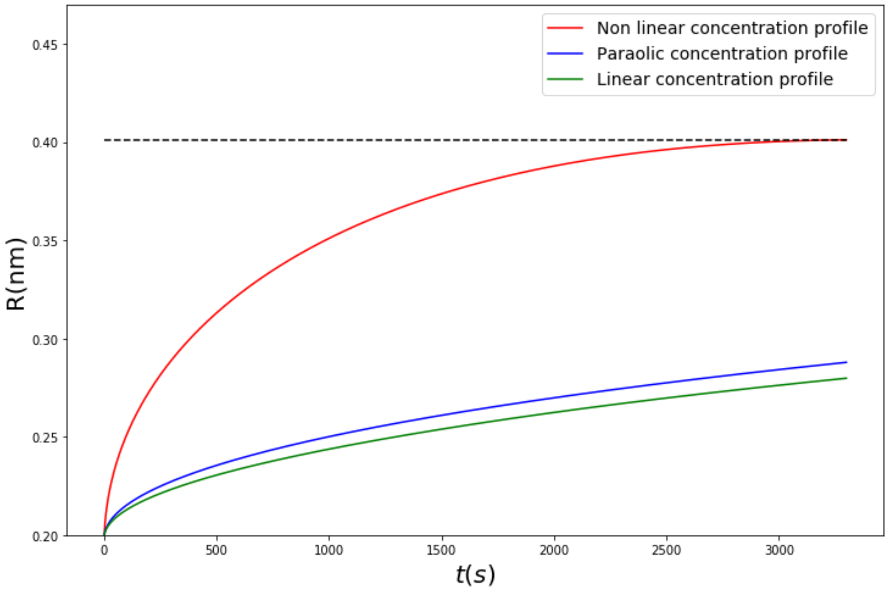

Figure 4.15: TiC precipitate growth according to the diffusional growth modal including soft impingement and the multi boundary model. The dotted line indicates $R_f = 0.401$ nm.

4.5.4. Single boundary model

The implementation of the single boundary model is the same as the single dislocation model. We make the same assumption as for the multi boundary model that the diffusion coefficient in the boundary (D_b) is the same as the diffusion coefficient in the pipe (D_p). Like the single dislocation model, we will analyze the effect of different values for D_b. The boundary thickness (δ) is assumed to be the same as the diameter of the dislocation pipe, and the average grain size (d_0) is assumed to be 20 µm. Both will be analyzed for different values. Table 4.12 shows the particle size at the end of tempering including and excluding the single boundary model. It shows results similar to those of the single dislocation model, where all concentration profile approximations have reached the maximum particle size before the end of tempering. Figure 4.16 shows the results of the soft impingement model, including the single boundary model. Since the growth is rapid, only the first 3 seconds are shown. The single boundary model seems to be the most assisting effect from the models used.

	R_{linear} (nm)	$R_{parabolic}$ (nm)	$R_{non-linear}$ (nm)
BN + SI	0.235	0.241	0.328
BN + SI + SB	0.401	0.401	0.401

Table 4.12: Precipitate size results. BN = Boundary nucleation, MN = Matrix nucleation, SI = soft impingement, SB = Single boundary model. The results for boundary nucleation are gained at $t = 3300$.

	t_{linear} (s)	$t_{parabolic}$ (s)	$t_{non-linear}$ (s)
SI + SB	2.22	2.69	2.89

Table 4.13: Time of growth until R_f is reached for the different concentration profile approximations. SI = soft impingement, SB = Single boundary model.

Table 4.13 shows the time for each concentration profile approximation, using the single boundary model, to reach R_f. Here we have a similar contradiction as before. The non-linear concentration profile seems to take the longest to reach R_f. In this case, the growth rate from the boundary is related to Ω. As seen in Figure 4.4, the non-linear concentration profile approximation will have the lowest $\Omega(c_s)$, next is the parabolic concentration profile approximation and the linear concentration profile approximation has the highest $\Omega(c_s)$. This explains the order in which the particles finish the growth stage. Unlike the single dislocation model, the difference growth rate from the boundary is not compensated in the difference in growth rate form the lattice so that the non-linear concentration profile approximation will be last. Figure 4.17 shows the change in the lattice and boundary growth from the single boundary model for the first 3 seconds of growth. We can see that, compared to the single dislocation model, the growth rate of the boundary is two orders of magnitude larger. In our case, the growth rate from the boundary dominates over the growth rate from the volume.

Figure 4.18 shows the effect of different ratios for $\frac{D_b}{D_l}$ on the growth of the precipitate using the non-linear

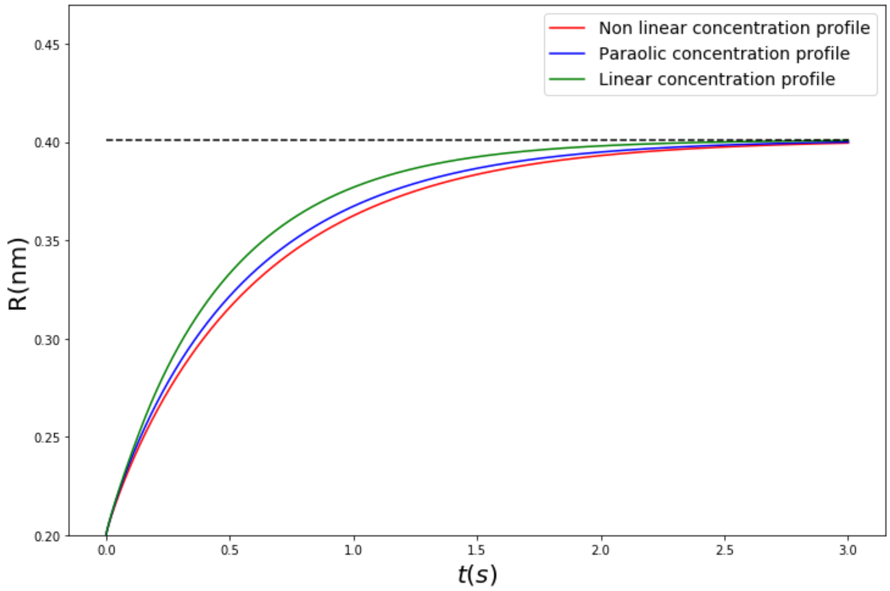

Figure 4.16: TiC precipitate growth according to the diffusional growth model including soft impingement and the single boundary model. The dotted line indicates $R_f = 0.401$ nm.

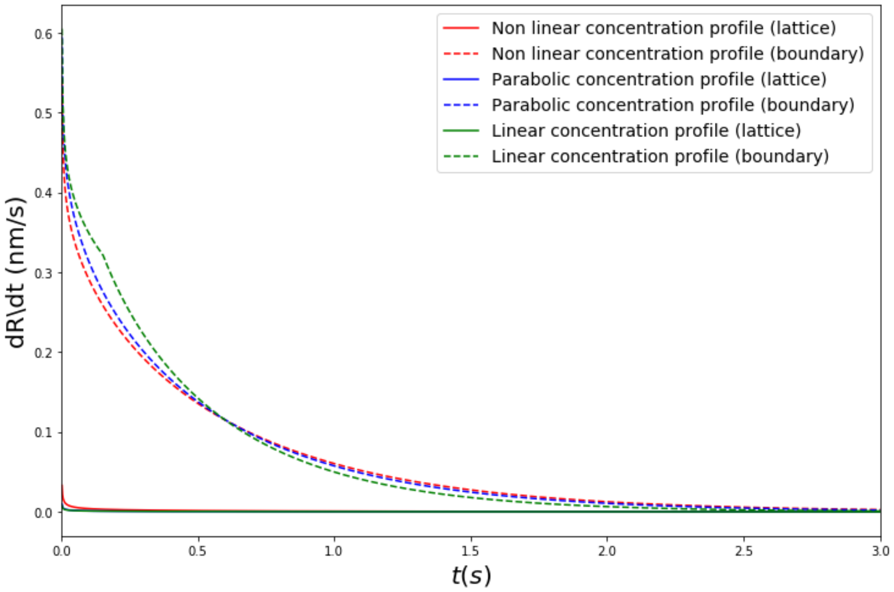

Figure 4.17: The lattice and boundary growth rate for all concentration profiles approximations from the single boundary model for the first 3 seconds of growth.

concentration profile approximation. With decreasing ratios, the growth rate decreases until it is almost similar to the growth rate excluding the single boundary model. Like the single dislocation model, when the diffusion coefficient of the solute in the pipe or boundary is equal to the diffusion coefficient in the lattice, there is still an assisted growth effect, due to the sum of diffusion from the same volume.

Figure 4.19 shows the analysis of different boundary thicknesses ranging from 0.2 to 2 nm. It shows that as the boundary thickness increases, the growth rate increases. We can conclude that setting the correct boundary thickness is important for the accuracy of the particle size. In our case, having a boundary thickness of 0.2 nm reaches R_f within 6.9 seconds, while having a thickness of 2 nm reaches R_f within 0.74 seconds.

Lastly, Figure 4.20 shows the effect of average grain size. Note that, to show the effect, $\frac{D_b}{D_l} = 10$ has been chosen. It seems that grain size only plays a role with a low diffusion coefficient. The grain sizes are 1, 10, 100, 1000 and ∞. Grains of this size are unrealistically small, but it visualizes the region where the grain size has an effect on the growth rate. Since grains this small are unrealistic, we can assume that the grain size has little to no effect on the growth of the precipitate using the single boundary model. Especially when $\frac{D_b}{D_l}$ is large. For the model, it is

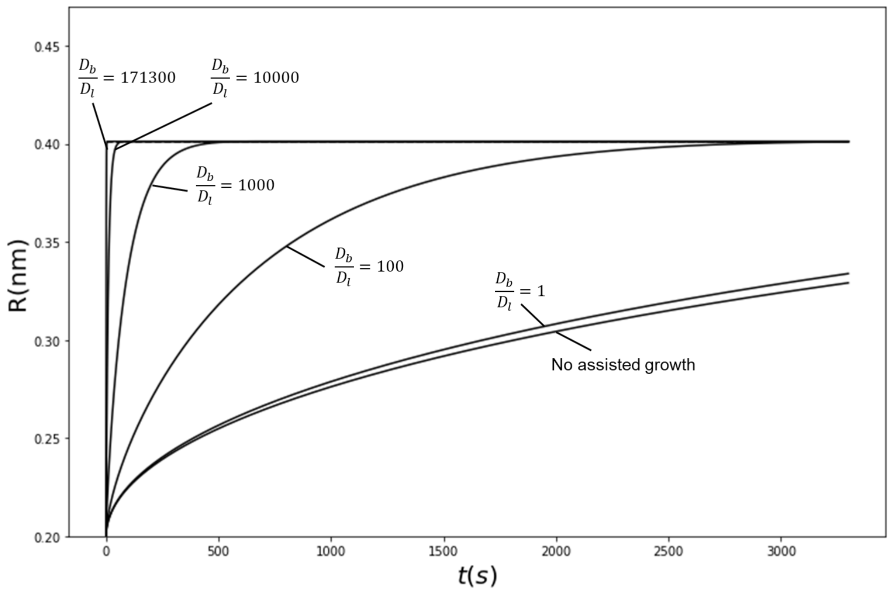

Figure 4.18: Effect of the boundary diffusion coefficient and lattice diffusion coefficient ratio ($\frac{D_b}{D_l}$) on the growth using the single boundary model.

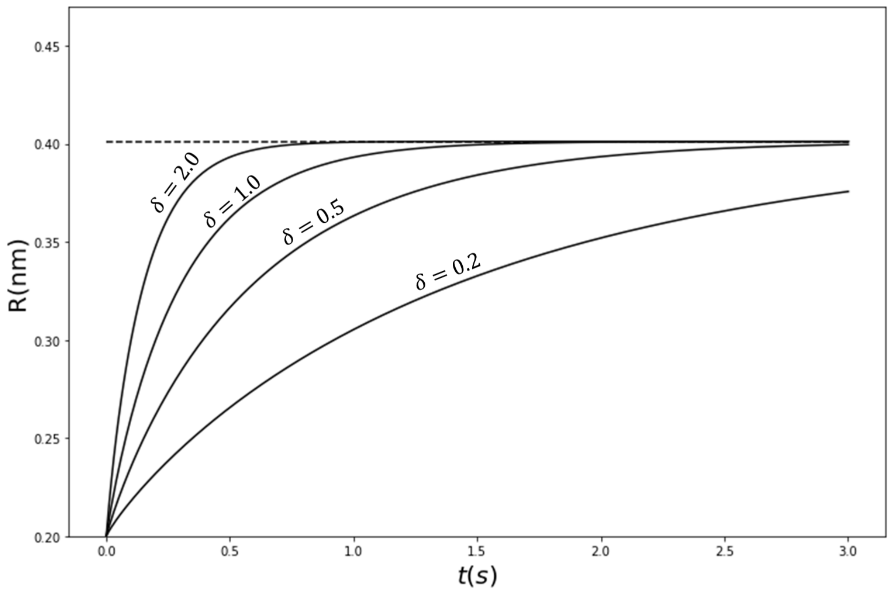

Figure 4.19: Effect of boundary thickness on the growth using the single boundary model.

reasonable to assume an infinitely large grain. No data of the grain size is needed and this simplifies the model by removing the middle term in equation (3.8) since β is equal to 0 for an infinitely large grain. This gives

$$\frac{dR}{dt}|_b = \Omega(\frac{\delta D_b}{4R^2} + (\frac{D_b}{\pi t})^{\frac{1}{2}}) \tag{4.2}$$

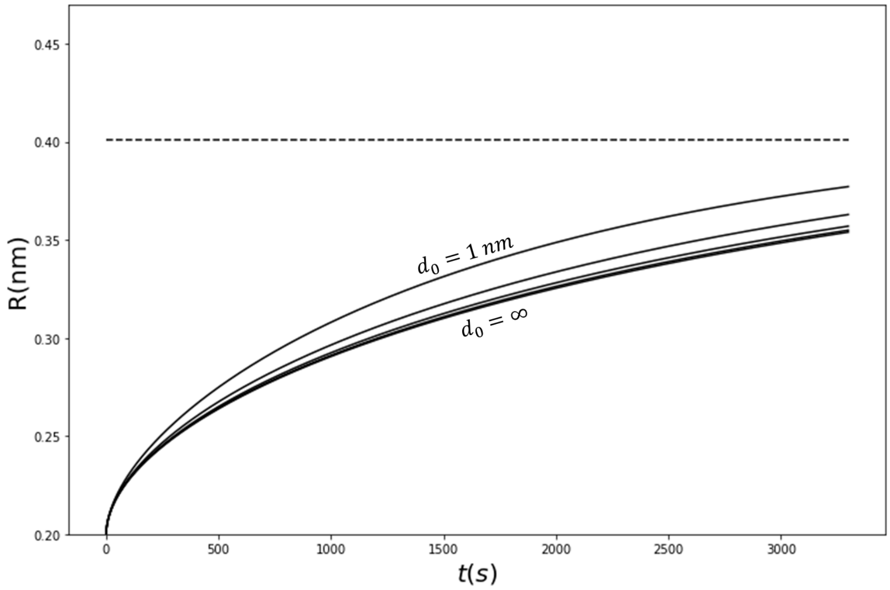

Figure 4.20: Effect of average grain size on the growth using the single boundary model. To show the effect $\frac{D_b}{D_l}$ = 10 has been chosen. The grain sizes are: 1, 10, 100, 1000 and ∞.

4.6. Application for TiC precipitation in martensitic steel [2]

Here, we compare our results with experimental data and the model used by Öhlund et al.. Two data sets will be presented. So far, we used x = 5nm as the average distance between the center of the initial particle and the middle between the initial particle and the neighboring particle. From the APT results [2], it shows that $x = 5 - 7.5$nm. Since the maximum particle size depends on x, we will show one set of results for $x = 5$ and one for $x = 7.5$. The data is presented in terms of the number of Ti atoms in the precipitate instead of particle size. We will convert the particle size to the number of atoms using the volume of one unit cell and the particle volume given by $V = 4/3\pi R^3$. If a particle contains one TiC unit cell, the particle contains 14 Ti atoms. If the unit cell is fully surrounded, it contains 4 Ti atoms. Any given unit cell will contain 4 to 14 Ti atoms. The results will be given in this range, where either all unit cells contain 4 or 14 Ti atoms. Also here, the Gibbs Thomson effect is not included, as it does not change the results.

4.6.1. Experimental data [2]

The APT results and the particle size according to the soft impingement model including and excluding assisted growth effects are shown in Table 4.14 and 4.15 for the linear, parabolic, and non-linear concentration profile approximation. Note that for boundary nucleation, the models allow the precipitate to grow for 55 min and for matrix nucleation for 30 - 50 min.

	VD	MD	SD	MB	SB	APT[2]
Linear: Boundary Nucl.	3 - 9	7 - 25	13 - 47	5 - 16	13 - 47	76 ± 48
Parabolic: Boundary Nucl.	3 - 10	8 - 27	13 - 47	5 - 17	13 - 47	76 ± 48
Non-linear: Boundary Nucl.	7 - 25	13 - 47	13 - 47	13 - 47	13 - 47	76 ± 48
Linear: Matrix Nucl.	2 - 9	4 - 23	13 - 47			35
Parabolic: Matrix Nucl.	2 - 10	5 - 25	13 - 47			35
Non-linear: Matrix Nucl.	5 - 24	13 - 47	13 - 47			35

Table 4.14: Precipitate size in number of Ti atoms for **x = 5nm**. VD = Volume diffusion, MD = Multi dislocation model, SD = Single dislocation model, MB = Multi boundary model, SB = Single boundary model.

Figures 4.21 and 4.22 show the particle size for the non-linear concentration profile approximation for x = 5nm and x = 7.5nm respectively. The volume diffusion model seems to underestimate the particle size for all concentration profiles. From this we can conclude that additional effects, such as dislocation or boundary assisted growth, play an important role in the particle growth. The strength of the assisted growth models is in the following order: Single boundary model < Single dislocation model < Multi dislocation model < Multi boundary model. In our case, the assisted growth models are all limited by R_f, especially when $x = 5nm$. Due to this limitation, the results are in reasonable agreement with the APT measurements.

	VD	MD	SD	MB	SB	APT[2]
Linear: Boundary Nucl.	3 - 9	8 - 27	45 - 157	5 - 16	45 - 157	76 ± 48
Parabolic: Boundary Nucl.	3 - 10	10 - 34	45 - 157	5 - 19	45 - 157	76 ± 48
Non-linear: Boundary Nucl.	9 - 30	44 - 156	45 - 157	26 - 92	45 - 157	76 ± 48
Linear: Matrix Nucl.	2 - 9	4 - 25	45 - 157			35
Parabolic: Matrix Nucl.	3 - 10	5 - 31	45 - 157			35
Non-linear: Matrix Nucl.	6 - 28	25 - 149	45 - 157			35

Table 4.15: Precipitate size in number of Ti atoms for **x = 7.5nm**. VD = Volume diffusion, MD = Multi dislocation model, SD = Single dislocation model, MB = Multi boundary model, SB = Single boundary model.

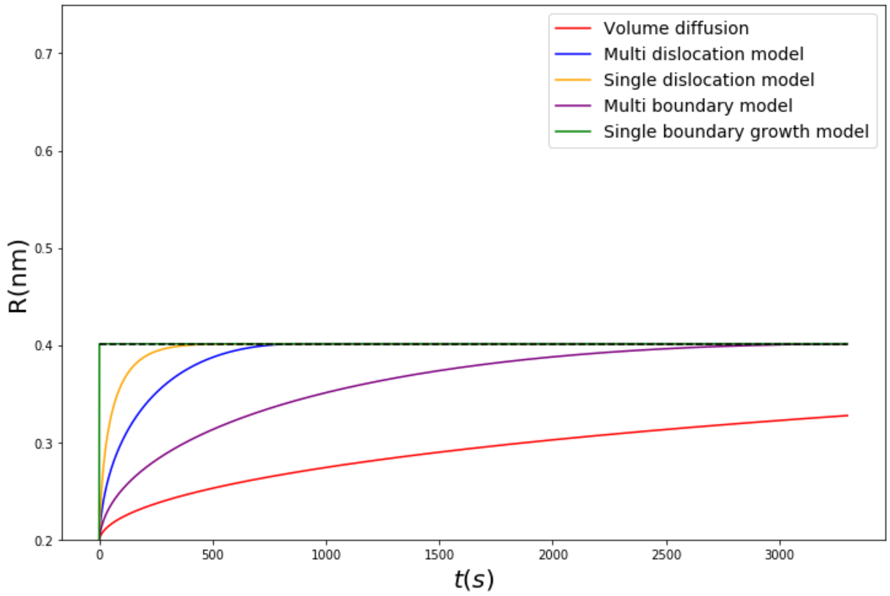

Figure 4.21: TiC Precipitate size for volume diffusion, multi dislocation model, single dislocation model, multi boundary model and the single boundary model for $x = 5nm$. The dotted line indicates $R_f = 0.401nm$.

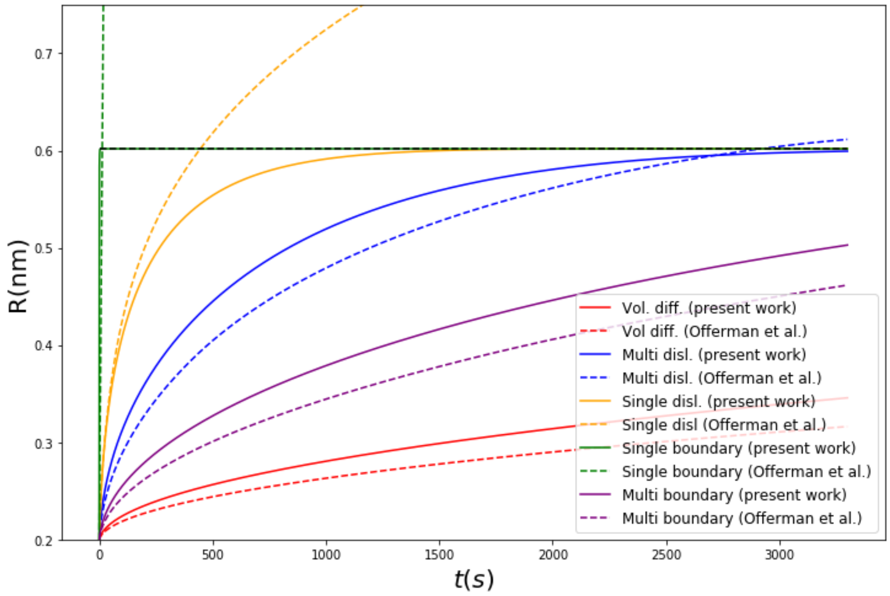

Figure 4.22: TiC Precipitate size for volume diffusion, multi dislocation model, single dislocation model, multi boundary model, and the single boundary model for $x = 7.5nm$. The dotted line indicates $R_f = 0.602nm$.

When we focus solely on volume diffusion, the non-linear concentration profile approximations seems the most accurate to the APT results. We have seen that at low supersaturation, the non-linear concentration profile is more accurate when compared to the exact solution. Using the linear or parabolic concentration profile approximation would underestimate the particle size, which could indicate a large effect of assisted growth by either dislocations of the boundary. This work shows that the assisted effect is still present but smaller when using the non-linear concentration profile approximation. When using one of the assisted growth models, it is important to have adequate data on the average half distance between particles (x) to prevent the assisted growth models from overestimating the particle size.

4.6.2. Model comparison [2]

In this part, we will compare our model with the soft impingement model used by Öhlund et al. [2] which is derived by Offerman et al. [3]. In this model, the parabolic growth constant (λ) is given by Zener's model [8] which is fitted to their data. This gives

$$\lambda = 2.102(\frac{c^{\infty} - c^{m}}{c^{p} - c^{\infty}})^{0.5871} \tag{4.3}$$

Which can be rewritten as

$$\lambda = 2.102(\frac{\Omega}{1 - \Omega})^{0.5871} \tag{4.4}$$

Note that this model does use the linear concentration profile for the calculation of c_s but not for the growth rate before soft impingement by measuring the parabolic growth constant with equation 4.4. We can compare this new approximation for λ with the concentration profile approximations. This is shown in Figures 4.23 and 4.24. This approach gives a more accurate solution than the linear and parabolic concentration profile approximation. At high supersaturation, it even gives larger values for λ than the exact solution and is even more accurate than the non-linear concentration profile approximation. But the non-linear concentration profile approximation is the most accurate at low supersaturation. The soft impingement effect is approximated in this model by using the intersection of the concentration profiles of the individual particles. In this model, the linear concentration profile approximation is used. The diffusion length is calculated using the mass balance, but without considering the presence of other particles. Using the diffusion length of the initial and neighboring particle, the intersection of the concentration profiles is calculated. It is assumed that c_s is located at

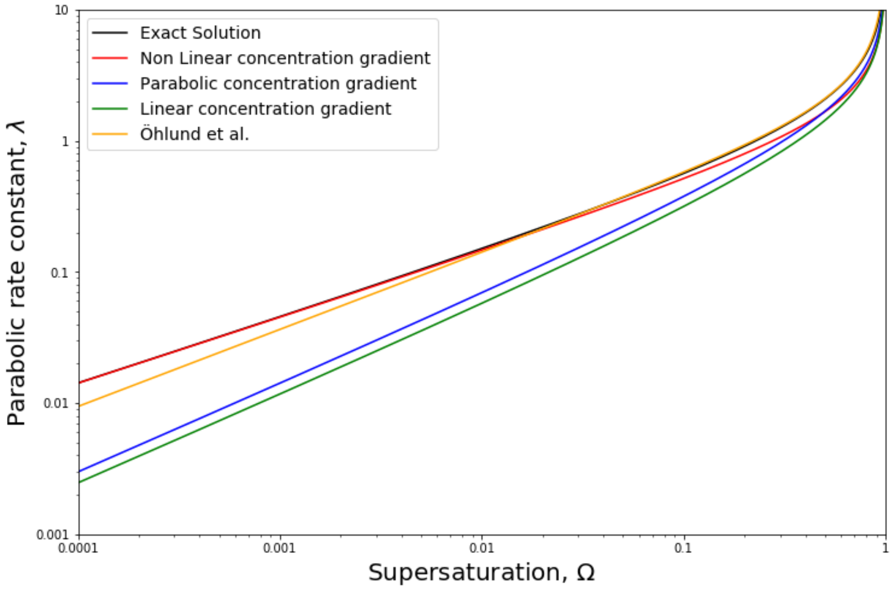

Figure 4.23: A comparison of λ for the exact solution, the concentration profile approximations and Zener's model used by Offerman et al. [3] and Öhlund et al.[2].

$$c_s = c_i(x,t) + c_a(x,t) - c^{\infty} \tag{4.5}$$

Where x is the half distance between the center of the initial and neighboring particle. For the linear concentration profile approximation, this gives

$$c_s = c^{\infty} - (c^{\infty} - c^{m})\frac{2R + 2L - 2x}{2L} \tag{4.6}$$

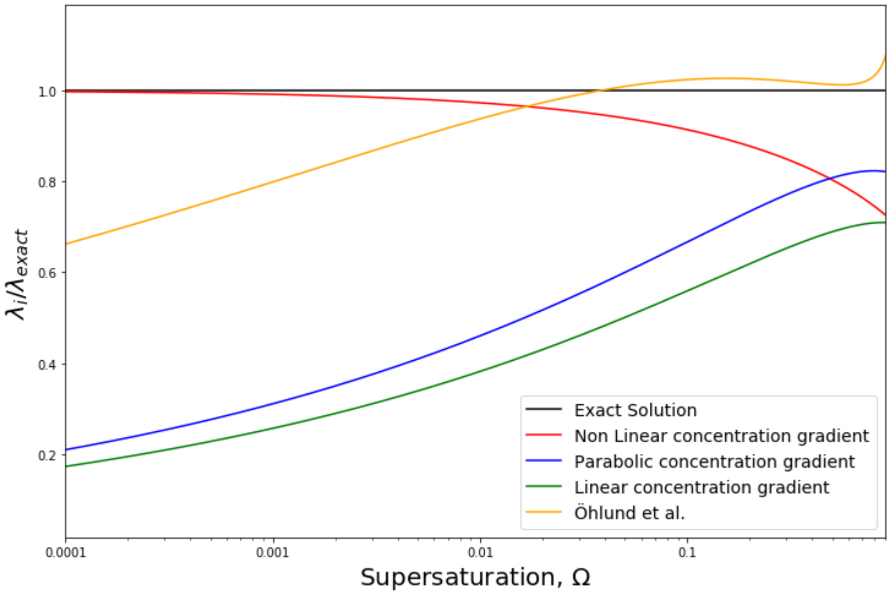

Figure 4.24: A comparison of λ for the exact solution, the concentration profile approximations and Zener's model used by Offerman et al. [3] and Öhlund et al.[2]. Normalized to λ of the exact solution.

In this model, soft impingement will start at the same point of the model in this thesis work, where the concentration profiles initially start to overlap. The growth of particles ends when $c_s = c^m$. It can be seen from equation (4.6) that particle growth ends when $R = x$, thus hard impingement occurs. This can overestimate the final particle size if enough time is given for growth.

	VD (nm)	MD (nm)	SD (nm)	MB (nm)	SB (nm)
Present work (non-linear)	0.327	0.401	0.401	0.401	0.401
Offerman et al.[3]	0.313	0.554	0.851	0.432	5.000

Table 4.16: Precipitate size (R) in nm for **x = 5nm**. The results show the particle size for boundary nucleation ($t = 55min$). VD = Volume diffusion, MD = Multi dislocation model, SD = Single dislocation model, MB = Multi boundary model, SB = Single boundary model.

	VD (nm)	MD (nm)	SD (nm)	MB (nm)	SB (nm)
Present work (non-linear)	0.346	0.599	0.602	0.503	0.602
Offerman et al.[3]	0.316	0.611	0.952	0.462	7.500

Table 4.17: Precipitate size (R) in nm for **x = 7.5nm**. The results show the particle size for boundary nucleation ($t = 55min$).

Tables 4.16 and 4.17 show the final precipitate size for the present model, using the non-linear concentration profile approximation, and the model of Offerman et al. [3] for $x = 5nm$ and $x = 7.5$nm respectively. Figures 4.25 and 4.26 show the precipitate size over time using both models for $x = 5nm$ and $x = 7.5$nm respectively. Two effects can be seen from the results. First, it shows that the present work gives a larger precipitate size for volume diffusion. This is due to the use of the non-linear concentration profile approximation, which gives a larger value for λ at the present supersaturation (Ω = 0.0005) than the approximation by Zener's model from equation (4.4) as seen in Figures 4.23 and 4.24. Secondly, when we add assisted growth effects, the present work gives a smaller precipitate size. This is due to the soft impingement effect which is included using different approximations in the model. In the present work, the particle cannot grow larger than R_f according to the mass balance. Whereas the model by Offerman et al.[3], the maximum particle size is reached on hard impingement. This happens when using the single boundary model. The multi and single dislocation model both have a particle size bigger than R_f and the multi boundary model has a particle size bigger than R_f when we use $x = 7.5nm$. In conclusion, The present model has a larger growth rate, but its limitation (preventing particles from growing beyond R_f) results in lower particle sizes when using the assisted growth models.

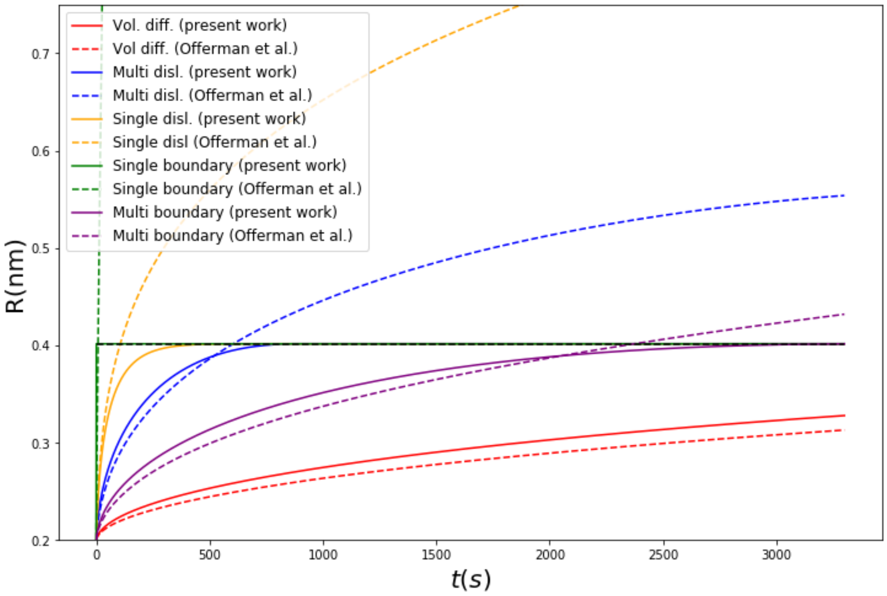

Figure 4.25: TiC Precipitate size for volume diffusion, multi dislocation model, single dislocation model, multi boundary model, and the single boundary model for $x = 5nm$. All solid lines indicate the present model using the non-linear concentration profile. The coloured dotted lines indicate the model by Offerman et al. [3]. The black dotted line indicates $R_f = 0.401nm$.

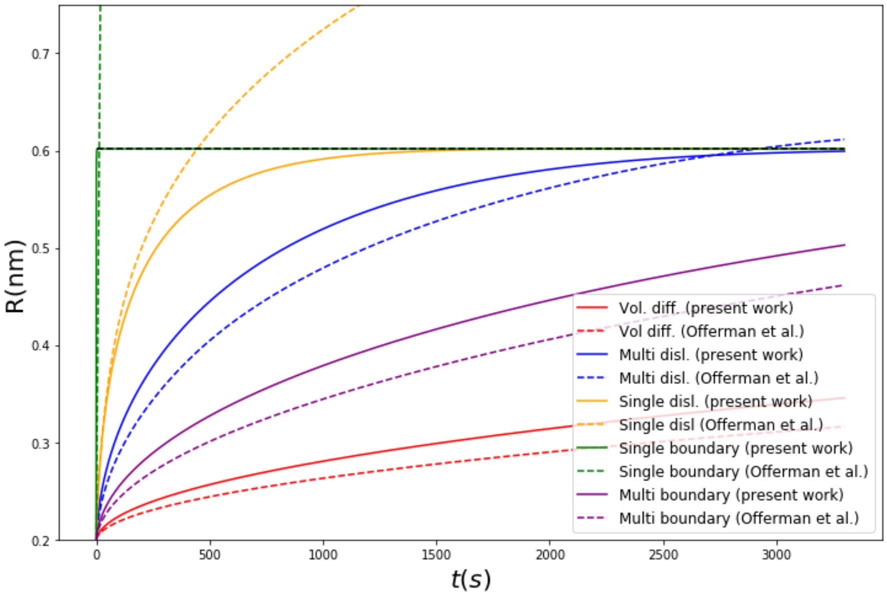

Figure 4.26: TiC Precipitate size for volume diffusion, multi dislocation model, single dislocation model, multi boundary model, and the single boundary model for $x = 7.5nm$. All solid lines indicate the present model using the non-linear concentration profile. The coloured dotted lines indicate the model by Offerman et al. [3]. The black dotted line indicates $R_f = 0.401nm$.

4.6.3. Limitations of the model

The main limitation of the model is that it can only predict an average particle size for all particles given a certain average distance between the particles. It can not give a distribution of expected particle sizes and does not include the effect of coarsening. Coarsening is an thermodynamically driven process, where large particles grow and smaller particles shrink. Larger particles have a smaller percentage of atoms on the surface compared to smaller particles, which makes them more stable.

The limitations of the model come from the assumptions we made in **Chapter 2.2**. First, we assumed that all particles nucleate at the same size. Secondly, we assumed that the particles are uniformly distributed. Because of this, the particles will all be the same size at any moment in time. This gives rise to the limitation in particle size of R_f. If the particles are not uniformly distributed, x would be different for each particle. Because of this R_f is also different for each particle. This then gives a distribution of particle sizes. An average distance x has to be calculated for every single particle. With this addition, the model would have to run for every single particle. The simulation time would be increased, depending on the amount of particles in the chosen volume element.

The model does not include the effect of coarsening. This can only be included if the particles have different sizes. Larger particles could take mass from smaller particles and from the matrix around them. The particles could then reach sizes larger than R_f. The particle size would no longer be limited by the amount of mass available in the matrix.

5

Conclusion and Recommendations

This thesis work aimed to model the effect of soft impingement for diffusion controlled growth of spherical particles with the implementation of the non-linear concentration profile approximation [1] to give accurate predictions of the particle size at low supersaturation. Additionally, the Gibbs Thomson effect [15] and assisted growth models like the multi dislocation model [16], the single dislocation model [17], the multi boundary model [18] and the single boundary model [19] are added.

Different concentration profile approximations are compared with the exact solution of the diffusional growth problem. The non-linear concentration profile approximation gives the most accurate results for $\Omega < 0.486$, while the parabolic concentration profile approximation is the most accurate for $\Omega > 0.486$. It is reasonable to use the non-linear concentration profile approximation for all values of Ω since the difference between the non-linear and parabolic concentration profile approximation is small for high supersaturation while it is large at low supersaturation. Also, the non-linear concentration profile approximation has a large diffusion length. Therefore, soft impingement will start much earlier compared to the linear and parabolic concentration profiles.

The model is applied to TiC precipitation in martensitic steel with $\Omega = 0.0005$. The non-linear concentration profile approximation gives the largest results for the particle size, then the parabolic concentration profile approximation and the linear concentration profile approximation give the smallest results, which is in agreement with the comparison of the three concentration profiles. The results for volume diffusion seem to underestimate the precipitate size, indicating the necessity to add the effect of dislocation or boundary assisted growth. Including assisted growth effects into the model gives results that are in reasonable agreement with experimental data [2] due to the precipitate radius reaching R_f before the end of tempering.

Additional effects on the soft impingement model are discussed and give the following results.

- The Gibbs Thomson effect does not seem to influence the results in the case of TiC precipitation in martensitic steel.
- The single boundary model has the highest growth rate, allowing the precipitate to reach R_f in seconds. The single dislocation model has the second largest growth rate, allowing the precipitate to reach R_f in 336 - 441 seconds, depending on the concentration profile approximation for $x = 5nm$. The multi dislocation model is next, allowing the precipitate to reach R_f in 723 seconds for the non-linear concentration profile approximation and does not reach R_f for the linear and parabolic concentration profile approximation due to the lower parabolic growth rate of those approximations. The multi boundary model has the smallest growth rate, where the non-linear concentration profile approximation reaches R_f in 2816 seconds.
- Using the multi dislocation and multi boundary model model show the same trend as the volume diffusion model when comparing the three concentration profile approximation. This is because this model only changes the diffusion coefficient (D) to the apparent diffusion coefficient (D_{app}) when dislocations are present.
- The single dislocation model and the boundary model do not show the same trend when comparing the different concentration profiles. For the boundary model, this is due to the fact that the growth rate of the boundary ($\frac{dR}{dt|_b}$) dominates the growth rate from the lattice or matrix ($\frac{dR}{dt}|_l$). $\frac{dR}{dt}|_b$ mainly depends on the value of c_s. c_s during soft impingement is largest for the linear concentration profile approximation, next is the parabolic, and last the non-linear. Because of this, the trend is the opposite for the boundary model, where the linear concentration profile approximation is fastest and the non-linear concentration profile

approximation is slowest. The single dislocation model has a mixed trend, where the growth rate of the dislocation ($\frac{dR}{dt}|_d$) is not completely dominant over $\frac{dR}{dt}|_l$. Because of this, the linear concentration profile approximation is fastest, next is the non-linear instead of the parabolic, because of the larger growth rate in the lattice for the non-linear concentration profile approximation.

- The effect of using different values for the diffusion coefficient in the dislocation pipe (D_p) is discussed.
- The effect of using different values for the diffusion coefficient in the boundary (D_b), the boundary thickness (δ) and average grain size (d_0) is discussed. Larger D_b and δ give larger particle sizes. It is reasonable to assume the average grain to be infinitely large, as it does not significantly change the results.

The present model is compared to the model used by Öhlund et al. [2]. In the case of TiC precipitation with $\Omega = 0.0005$, the present model with the non-linear concentration profile approximation gives a larger precipitate size for volume diffusion due to having a larger parabolic growth constant (λ) when using the non-linear concentration profile approximation instead of Zener's approximation [8]. The present model gives a smaller precipitate size for the assisted growth models. This is because the precipitates in the model used by Öhlund et al. can reach a size larger than R_f. The comparison indicates the importance of including a maximum precipitate size according to the mass balance.

The limitations of the model are presented. It can not give an expected particle distribution but only one size and the effect of coarsening is not included. Based on the limitations, future recommendations for further improving the soft impingement model are defined as followed.

- The assumption of uniform distribution could be removed. This includes that the model should run for every single particle in the chosen volume element. x can be defined individually for each particle based on the distances from its neighbouring particles. As a result, this would give a particle size distribution instead of an average particle size.
- The assumption where all particles nucleate at the same time could be removed. If particles nucleate at different times, the particles will also reach different sizes giving a particle size distribution. If this assumption is removed together with the previous one, then x needs to be calculated over time. New particles can nucleate next to existing ones, decreasing the average distance between neighbouring particles.
- The effect of coarsening can be included to allow bigger particles to grow, even when R_f is reached, and smaller ones to shrink.

References

1. Seki, A. & Hayashi, K. A New Approximate Solution for Diffusional Growth and Dissolution of Spherical Precipitates. *MATERIALS TRANSACTIONS* **62,** 161–166 (2021).
2. Öhlund, C. E. I. C., Weidow, J., Thuvander, M. & Offerman, S. E. Effect of Ti on Evolution of Microstructure and Hardness of Martensitic Fe–C–Mn Steel during Tempering. *ISIJ International* **54,** 2890–2899 (2014).
3. Offerman, S. *et al.* Solid-state phase transformations involving solute partitioning: modeling and measuring on the level of individual grains. *Acta Materialia* **52,** 4757–4766. ISSN: 1359-6454 (2004).
4. Chen, H. & van der Zwaag, S. Modeling of soft impingement effect during solid-state partitioning phase transformations in binary alloys. *J Mater Sci* **46,** 1328–1336 (2011).
5. Offerman, S. Presentation slides: Dislocation Interactions and Applications. *TU Delft Course: Metal Science II* (2023).
6. Mehl, R. F. & Dubé, C. Phase Transformations in Solids. *John Wiley* (1951).
7. Hubert I. Aaronson Masato Enomoto, J. K. L. *Mechanisms of Diffusional Phase Transformations in Metals and Alloys* (CRC Press, 2010).
8. Zener & Clarence. Theory of Growth of Spherical Precipitates from Solid Solution. *Journal of Applied Physics* **20,** 950–953. ISSN: 0021-8979. `https://doi.org/10.1063/1.1698258` (Oct. 1949).
9. Aaron, H. B., Fainstein, D. & Kotler, G. R. Diffusion-Limited Phase Transformations: A Comparison and Critical Evaluation of the Mathematical Approximations. *Journal of Applied Physics* **41,** 4404–4410. ISSN: 0021-8979. `https://doi.org/10.1063/1.1658474` (Oct. 1970).
10. Mullins, W. W. & Sekerka, R. F. Morphological Stability of a Particle Growing by Diffusion or Heat Flow. *Journal of Applied Physics* **34,** 323–329. ISSN: 0021-8979. `https://doi.org/10.1063/1.1702607` (Feb. 1963).
11. Fan, K. *et al.* Modeling of isothermal solid-state precipitation using an analytical treatment of soft impingement. *Acta Materialia* **56,** 4309–4318. ISSN: 1359-6454. `https://www.sciencedirect.com/science/article/pii/S1359645408003364` (2008).
12. De Andrés, C. G., Capdevila, C., Caballero, F. & Bhadeshia, H. Moddeling of isothermal ferrite formation using an analytical treatment of soft impingement in 0.37C–1.45Mn–0.11V steel. *Acta Metallurgica* (1998).
13. Wang, H., Liu, F., Zhang, T., Yang, G. & Zhou, Y. Kinetics of diffusion-controlled transformations: Application of probability calculation. *Acta Materialia* **57,** 3072–3083. ISSN: 1359-6454 (2009).
14. Fang, H., van der Zwaag, S. & van Dijk, N. A novel 3D mixed-mode multigrain model with efficient implementation of solute drag applied to austenite-ferrite phase transformations in Fe-C-Mn alloys. *Acta Materialia* **212,** 116897 (2021).
15. Perez, M. Gibbs–Thomson effects in phase transformations. *Scripta Materialia* **52,** 709–712. ISSN: 1359-6462 (2005).
16. Porter, D. A. & Easterling, K. E. *Phase Transformations in Metals and Alloys* 102 (Van Nostrand Reinhold, 1981).
17. Wang, Z. & Shiflet, G. Growth of δ' on dislocations in a dilute Al-Li alloy. *Metall Mater Trans A* **29,** 2073–2085 (1998).
18. Santofimia, M. J. & Sietsma, J. *Microstructure Control in Metals* 121–122 (Self-published, 2022).
19. Cheng, L., Hawbolt, E. & Meadowcroft, T. Modeling of dissolution, growth, and coarsening of aluminum nitride in low-carbon steels. *Metallurgical and Materials Transactions A: Physical Metallurgy and Materials Science* **31,** 1907–1916 (Aug. 2000).
20. Polte, J. Fundamental growth principles of colloidal metal nanoparticles – a new perspective. *CrystEngComm* (2015).
21. Shima, Y. *et al.* Self-Diffusion along Dislocations in Ultra High Purity Iron. *Mater. Trans,* **43** (2002).
22. J.O., A., T., H., L., H., P.F., S. & B., S. Thermo-Calc and DICTRA, Computational tools for materials science. *Calphad* (2002).
23. Incropera, F. & deWitt, D. P. *Fundamentals of Heat and Mass Transfer* (Wiley, 1985).

A

Appendix

A.1. Calculation for R_f

To calculate R_f we will use a 3D mass balance. Note that we can not use the same mass balance with the calculation of R_c ($R_f + L = x$), since L loses its meaning after soft impingement.

The 3D mass balance

$$\int_0^{R_f} c^p 4\pi r^2 dr + \int_{R_f}^{x} c^m 4\pi r^2 dr = \int_0^{x} c^\infty 4\pi r^2 dr \tag{A.1}$$

Now we solve for R_f

$$\int_0^{R_f} c^p 4\pi r^2 dr + \int_{R_f}^{x} c^m 4\pi r^2 dr = \int_0^{x} c^\infty 4\pi r^2 dr \tag{A.2}$$

$$\int_0^{R_f} c^p r^2 dr + \int_{R_f}^{x} c^m r^2 dr = \int_0^{x} c^\infty r^2 dr \tag{A.3}$$

$$\frac{1}{3} c^p {R_f}^3 + \frac{1}{3} c^m (x^3 - {R_f}^3) = \frac{1}{3} c^\infty x^3 \tag{A.4}$$

$$c^p {R_f}^3 + c^m (x^3 - {R_f}^3) = c^\infty x^3 \tag{A.5}$$

$$c^p {R_f}^3 + c^m x^3 - c^m {R_f}^3 = c^\infty x^3 \tag{A.6}$$

$$(c^p - c^m) \frac{{R_f}^3}{x^3} = c^\infty - c^m \tag{A.7}$$

$$\frac{{R_f}^3}{x^3} = \frac{c^\infty - c^m}{c^p - c^m} = \Omega \tag{A.8}$$

$$R_f^3 = x^3 \Omega \tag{A.9}$$

$$R_f = x \Omega^{\frac{1}{3}} \tag{A.10}$$

An other way to solve for R_f is by the use of the following mass balance

$$\frac{4}{3} \pi {R_f}^3 (c^p - c^\infty) = \frac{4}{3} \pi (x^3 - {R_f}^3)(c^\infty - c^m) \tag{A.11}$$

Again, we solve for R_f:

$$\frac{4}{3} \pi {R_f}^3 (c^p - c^\infty) = \frac{4}{3} \pi (x^3 - {R_f}^3)(c^\infty - c^m) \tag{A.12}$$

$${R_f}^3 (c^p - c^\infty) = (x^3 - {R_f}^3)(c^\infty - c^m) \tag{A.13}$$

$$\frac{{R_f}^3}{(x^3 - {R_f}^3)} = \frac{(c^\infty - c^m)}{(c^p - c^\infty)} \tag{A.14}$$

$${R_f}^3 = x^3 * \frac{(c^\infty - c^m)}{(c^p - c^\infty)} - {R_f}^3 * \frac{(c^\infty - c^m)}{(c^p - c^\infty)} \tag{A.15}$$

$$R_f{}^3 + R_f{}^3 * \frac{(c^\infty - c^m)}{(c^p - c^\infty)} = x^3 * \frac{(c^\infty - c^m)}{(c^p - c^\infty)} \tag{A.16}$$

$$R_f{}^3 * (1 + \frac{(c^\infty - c^m)}{(c^p - c^\infty)}) = x^3 * \frac{(c^\infty - c^m)}{(c^p - c^\infty)} \tag{A.17}$$

$$R_f{}^3 = x^3 * \frac{\frac{(c^\infty - c^m)}{(c^p - c^\infty)}}{\frac{(c^\infty - c^m)}{(c^p - c^\infty)} + 1} \tag{A.18}$$

We rewrite the last term using $(c^p - c^m) = (c^p - c^\infty) + (c^\infty - c^m)$.

$$\frac{\frac{(c^\infty - c^m)}{(c^p - c^\infty)}}{\frac{(c^\infty - c^m)}{(c^p - c^\infty)} + 1} = \frac{\frac{(c^p - c^m) - (c^p - c^\infty)}{(c^p - c^\infty)}}{\frac{(c^p - c^m) - (c^p - c^\infty)}{(c^p - c^\infty)} + 1} = \frac{\frac{(c^p - c^m)}{(c^p - c^\infty)} - 1}{\frac{(c^p - c^m)}{(c^p - c^\infty)}} = 1 - \frac{(c^p - c^\infty)}{(c^p - c^m)} = \frac{(c^\infty - c^m)}{(c^p - c^m)} = \Omega \tag{A.19}$$

This gives

$$R_f{}^3 = x^3\Omega \tag{A.20}$$

$$R_f = x\Omega^{\frac{1}{3}} \tag{A.21}$$

A.2. Calculations for c_s

To get a function for c_s, we solve the following mass balance

$$\int_0^R c^p 4\pi r^2 dr + \int_R^x c(r,t) 4\pi r^2 dr = \int_0^x c_0^\infty 4\pi r^2 dr \tag{A.22}$$

$$\int_0^R c^p r^2 dr + \int_R^x c(r,t) r^2 dr = \int_0^x c_0^\infty r^2 dr \tag{A.23}$$

$$\frac{1}{3} c^p R^3 + \int_R^x c(r,t) r^2 dr = \frac{1}{3} c_0^\infty x^3 \tag{A.24}$$

$$\int_R^x c(r,t) r^2 dr = \frac{1}{3} c_0^\infty x^3 - \frac{1}{3} c^p R^3 \tag{A.25}$$

From here, we replace $c(r,t)$ with the function of the concentration profile and solve the integral on the left.

A.2.1. Linear concentration profile

For the linear concentration profile approximation we will use

$$\int_R^x c(r,t) r^2 dr = \int_R^x (\frac{c_s - c^m}{x - R}(r - R) + c^m) r^2 dr = \tag{A.26}$$

$$\int_R^x r^3 \frac{c_s - c^m}{x - R} - r^2 R \frac{c_s - c^m}{x - R} + r^2 c^m dr = \tag{A.27}$$

$$\int_R^x r^3 \frac{c_s - c^m}{x - R} dr - \int_R^x r^2 R \frac{c_s - c^m}{x - R} dr + \int_R^x r^2 c^m dr = \tag{A.28}$$

$$(c_s - c^m) \frac{1}{x - R} \int_R^x r^3 dr - (c_s - c^m) \frac{R}{x - R} \int_R^x r^2 dr + c^m \int_R^x r^2 dr = \tag{A.29}$$

$$(c_s - c^m) \frac{1}{x - R} \frac{1}{4}(x^4 - R^4) - (c_s - c^m) \frac{R}{x - R} \frac{1}{3}(x^3 - R^3) + c^m \frac{1}{3}(x^3 - R^3) = \tag{A.30}$$

$$(c_s - c^m)(\frac{1}{x - R} \frac{1}{4}(x^4 - R^4) - \frac{R}{x - R} \frac{1}{3}(x^3 - R^3)) + c^m \frac{1}{3}(x^3 - R^3) \tag{A.31}$$

$$\frac{1}{3}(c_s - c^m) A_1 + c^m \frac{1}{3}(x^3 - R^3) \tag{A.32}$$

with

$$A_1 = 3(\frac{1}{x - R} \frac{1}{4}(x^4 - R^4) - \frac{R}{x - R} \frac{1}{3}(x^3 - R^3)) \tag{A.33}$$

Now we insert equation (A.32) into equation (A.25).

$$\frac{1}{3}(c_s - c^m)A_1 + c^m\frac{1}{3}(x^3 - R^3) = \frac{1}{3}c_0^\infty x^3 - \frac{1}{3}c^p R^3 \tag{A.34}$$

$$(c_s - c^m)A_1 = c_0^\infty x^3 - c^p R^3 - c^m(x^3 - R^3) \tag{A.35}$$

$$(c_s - c^m)A_1 = x^3(c_0^\infty - c^m) + R^3(c^m - c^p) \tag{A.36}$$

$$c_s = \frac{x^3(c_0^\infty - c^m) + R^3(c^m - c^p)}{A_1} + c^m \tag{A.37}$$

A.2.2. Parabolic concentration profile

For the linear concentration profile approximation we will use

$$\int_R^x c(r,t)r^2dr = \int_R^x (c^m - 2\frac{c_s - c^m}{x - R}(r - R) + \frac{c_s - c^m}{(x-R)^2}(r - R)^2)r^2dr = \tag{A.38}$$

$$\int_R^x c^m r^2 - (c_s - c^m)(2(\frac{r-R}{x-R}) - (\frac{r-R}{x-R})^2)r^2dr = \tag{A.39}$$

$$\int_R^x c^m r^2 - (c_s - c^m)(2(\frac{r-R}{x-R}) - (\frac{r-R}{x-R})^2)r^2dr = \tag{A.40}$$

$$\int_R^x c^m r^2 - (c_s - c^m)(\frac{2r}{x-R} - \frac{2R}{x-R} - (\frac{r^2}{(x-R)^2} - \frac{2rR}{(x-R)^2} + \frac{R^2}{(x-R)^2}))r^2dr = \tag{A.41}$$

$$\int_R^x c^m r^2 - (c_s - c^m)(\frac{2}{x-R}(r - R) - \frac{1}{(x-R)^2}(r^2 - 2rR + R^2))r^2dr = \tag{A.42}$$

$$\int_R^x c^m r^2 - (c_s - c^m)(\frac{2}{x-R}(r^3 - r^2R) - \frac{1}{(x-R)^2}(r^4 - 2r^3R + r^2R^2))dr = \tag{A.43}$$

$$\frac{1}{3}c^m(x^3 - R^3) + (c_s - c^m)(\frac{2}{x-R}(\frac{1}{4}(x^4 - R^4) - \frac{1}{3}R(x^3 - R^3)) - \frac{1}{(x-R)^2}(\frac{1}{5}(x^5 - R^5) - \frac{1}{2}R(x^4 - R^4) + \frac{1}{3}R^2(x^3 - R^3))) = \tag{A.44}$$

$$\frac{1}{3}(c_s - c^m)A_2 + \frac{1}{3}c^m(x^3 - R^3) \tag{A.45}$$

with

$$A_2 = 3(\frac{2}{x-R}(\frac{1}{4}(x^4 - R^4) - \frac{1}{3}R(x^3 - R^3)) - \frac{1}{(x-R)^2}(\frac{1}{5}(x^5 - R^5) - \frac{1}{2}R(x^4 - R^4) + \frac{1}{3}R^2(x^3 - R^3))) \tag{A.46}$$

Now we insert equation (A.45) into equation (A.25).

$$\frac{1}{3}(c_s - c^m)A_2 + \frac{1}{3}c^m(x^3 - R^3) = \frac{1}{3}c_0^\infty x^3 - \frac{1}{3}c^p R^3 \tag{A.47}$$

$$(c_s - c^m)A_2 = c_0^\infty x^3 - c^p R^3 - c^m(x^3 - R^3) \tag{A.48}$$

$$(c_s - c^m)A_2 = x^3(c_0^\infty - c^m) + R^3(c^m - c^p) \tag{A.49}$$

$$c_s = \frac{x^3(c_0^\infty - c^m) + R^3(c^m - c^p)}{A_2} + c^m \tag{A.50}$$

A.2.3. Non-linear concentration profile

For the non-linear concentration profile approximation we will use

$$\int_R^x c(r,t)r^2dr = \int_R^x ((c^m - c_s)\frac{R}{r}(1 - \frac{r-R}{x-R}) + c_s)r^2dr = \tag{A.51}$$

$$\int_R^x ((c^m - c_s)\frac{R}{r}(1 - \frac{r-R}{x-R})r^2 + c_s r^2)dr = \tag{A.52}$$

$$\int_R^x ((c^m - c_s)(1 - \frac{r-R}{x-R})Rr + c_s r^2)dr = \tag{A.53}$$

$$\int_R^x (((c^m - c_s)Rr - (c^m - c_s)(\frac{r-R}{x-R})Rr + c_s r^2)dr = \tag{A.54}$$

$$\int_R^x (c^m - c_s)Rrdr - \int_R^x (c^m - c_s)(\frac{r-R}{x-R})Rrdr + \int_R^x c_s r^2dr = \tag{A.55}$$

$$\int_R^x (c^m - c_s)Rrdr - \int_R^x ((c^m - c_s)(\frac{Rr^2}{x-R}) - (c^m - c_s)(\frac{R^2r}{x-R}))dr + \int_R^x c_s r^2dr = \tag{A.56}$$

$$\int_R^x (c^m - c_s)Rrdr - \frac{(c^m - c_s)}{x-R}\int_R^x (Rr^2 - R^2r))dr + \int_R^x c_s r^2dr = \tag{A.57}$$

$$\int_R^x (c^m - c_s)Rrdr - \frac{(c^m - c_s)}{x-R}(\int_R^x Rr^2dr - \int_R^x R^2rdr) + \int_R^x c_s r^2dr = \tag{A.58}$$

$$\frac{1}{2}(c^m - c_s)(x^2 - R^2)R - \frac{(c^m - c_s)}{x-R}(\frac{1}{3}(x^3 - R^3)R - \frac{1}{2}(x^2 - R^2)R^2) + \frac{1}{3}c_s(x^3 - R^3) \tag{A.59}$$

$$(c^m - c_s)(\frac{1}{2}(x^2 - R^2)R - \frac{1}{x-R}(\frac{1}{3}(x^3 - R^3)R - \frac{1}{2}(x^2 - R^2)R^2)) + \frac{1}{3}c_s(x^3 - R^3) \tag{A.60}$$

$$\frac{1}{3}(c^m - c_s)A_3 + \frac{1}{3}c_s(x^3 - R^3) \tag{A.61}$$

with

$$A_3 = 3(\frac{1}{2}(x^2 - R^2)R - \frac{1}{x-R}(\frac{1}{3}(x^3 - R^3)R - \frac{1}{2}(x^2 - R^2)R^2)) \tag{A.62}$$

Now we insert equation (A.61) into equation (A.25).

$$\frac{1}{3}(c^m - c_s)A_3 + \frac{1}{3}c_s(x^3 - R^3) = \frac{1}{3}c_0^\infty x^3 - \frac{1}{3}c^pR^3 \tag{A.63}$$

$$c_s(x^3 - R^3) - c_sA_3 = c_0^\infty x^3 - c^pR^3 - c^mA_3 \tag{A.64}$$

$$c_s(x^3 - R^3 - A_3) = c_0^\infty x^3 - c^pR^3 - c^mA_3 \tag{A.65}$$

$$c_s = \frac{c_0^\infty x^3 - c^pR^3 - c^mA_3}{x^3 - R^3 - A_3} \tag{A.66}$$

A.3. Gibbs Thomson Effect

In this part, the origin of the Gibbs Thomson effect is explained. This will lead to the general form of the Gibbs-Thomson equation.

For this derivation we will assume a binary mixture of atoms A and B [18]. Let's first assume no precipitate (phase β) is present and only phase α is present. The Gibbs free energy for mixing the two elements is given by

$$G^\alpha = X_AG_A + X_BG_B + \Delta G_{mix} \tag{A.67}$$

Where X_A and X_B are the fractions A and B, G_A and G_B are the Gibbs free energy of a pure system of A and B respectively and ΔG_{mix} is the change in energy due to mixing. ΔG_{mix} is given as

$$\Delta G_{mix} = \Delta H_{mix} - T\Delta S_{mix} \tag{A.68}$$

Where ΔH_{mix} and ΔS_{mix} or the enthalpy and entropy of mixing. To define ΔH_{mix}, we assume a homogeneous distribution of elements and the enthalpy effects are only approximated with closed neighbor bonds (AA, AB, BB). Then ΔH_{mix} is given as

$$\Delta H_{mix} = \Omega X_A X_B \tag{A.69}$$

Where Ω is the regular solution parameter given as

$$\Omega = n_{av} z(\varepsilon_{AB} - \frac{1}{2}(\varepsilon_{AA} + \varepsilon_{BB})) \tag{A.70}$$

Where n_{av} is Avogadro's constant, z is the coordination number and ε_{ij} is the binding energy between atoms i and j. Here, $\frac{1}{2}n_{av}z$ is the amount of bonds in the system but is multiplied by two in this equation due to the probability of A-B bond to occur in a randomly mixed system being equal to $2X_AX_B$. The right term $(\varepsilon_{AB} - \frac{1}{2}(\varepsilon_{AA} + \varepsilon_{BB}))$, is the difference enthalpy due to the creation of an A-B from the reaction: $\frac{1}{2}AA + \frac{1}{2}BB \longrightarrow AB$. To define ΔS_{mix}, we assume that the thermal entropy, which is related to the number of ways in which vibrations can occur in the solid, is negligible compared to the configurations enthalpy, which is related to the number of ways atoms A and B can be arranged on the lattice. Also all configurations of A and B are equally probable. ΔS_{mix} can be given as

$$\Delta S_{mix} = k\ ln(\omega) \tag{A.71}$$

Where ω is the number of ways the atoms can be arranged on the lattice given by the number of possible ways to arrange A and B atoms ($(n_A + n_B)!$) reduced by $n_A!n_B!$ since all A and all B atoms are the same to each other, given by

$$\omega = \frac{(n_A + n_B)!}{n_A!n_B!} \tag{A.72}$$

Where n_A and n_B are the amount of atoms A and B. Using Stirling's mathematical approximation ($ln(n!) = n\ ln(n) - n$) and the relations $n_i = X_i n$ and $R = kn_{av}$, ΔS_{mix} can be rewritten as

$$\Delta S_{mix} = -R(X_A ln(X_A) + X_B ln(X_B)) \tag{A.73}$$

G^α can then be written as

$$G^\alpha = G_A X_A + G_B X_B + \Omega X_A X_B + RT(X_A ln(X_A) + X_B ln(X_B)) \tag{A.74}$$

For the derivation of the Gibbs-Thomson equation we use the article by Perez [15]. G^α can be rewritten using $X_i = \frac{n_i}{n_i + n_j}$.

$$G^\alpha = n_A(G_A + kTln(\frac{n_A}{n_A + n_B})) + n_B(G_B + kTln(\frac{n_B}{n_A + n_B})) + \Omega(\frac{n_A n_B}{n_A + n_B}) \tag{A.75}$$

We add another phase (β) of composition A_xB_y where the molar concentration for B is equal to $X_p = \frac{y}{x+y}$, the free Gibbs energy is

$$G^\beta = n^\beta G_n^\beta \tag{A.76}$$

Where n^β is the amount of atoms in the β phase and G_n^β is the free energy per atom. If both phases are in equilibrium at the interface, transferring atoms A and B from phase α (composition X_0^m) to β (composition X_p) will not change the total energy of the system. This can be given as

$$dn(1 - X_p)\frac{\delta G^\alpha}{\delta n_A^\alpha} + dnX_p\frac{\delta G^\alpha}{\delta n_B^\alpha} = dn\frac{\delta G^\beta}{\delta n} \tag{A.77}$$

Solving this for a dilute regular solution gives

$$G_n^\beta = (1 - X_p)[G_A^\alpha + kTln(1 - X_0^m)] + X_p[G_B^\alpha + \Omega + kTln(X_0^m)] \tag{A.78}$$

Here, the interracial energy is not taking into account. A term for the interfacial energy needs to be added to A.76 to derive the new equilibrium condition.

$$G^\beta = n^\beta G_n^\beta + \gamma S^\beta \tag{A.79}$$

Where γ is the surface energy and S^β is the surface area. The β phase is assumed to be spherical with radius r and atomic volume v_{at}^β.

$$\frac{4}{3}\pi r^3 = n^\beta v_{at}^\beta \tag{A.80}$$

$\frac{\delta G^\beta}{\delta n^\beta}$ is then given by

$$\frac{\delta G^\beta}{\delta n^\beta} = G_n^\beta + \frac{2\gamma v_{at}^\beta}{r} \tag{A.81}$$

The new equilibrium condition between phase α (composition $X^m(r)$) and phase β (composition X^p) is then given by

$$G_n^\beta + \frac{2\gamma v_{at}^\beta}{r} = (1 - X_p)[G_A^\alpha + kTln(1 - X^m(r))] + X_p[G_B^\alpha + \Omega + kTln(X^m(r))] \tag{A.82}$$

Now we subtract the equation with (A.82) and without (A.78) the interfacial energy term to get the general form of the Gibbs-Thomson equation.

$$\frac{2\gamma v_{at}^\beta}{rkT} = (1 - X^p)ln(\frac{1 - X^m(r)}{1 - X_0^m}) + X^p ln(\frac{X^m(r)}{X_0^m}) \tag{A.83}$$

or

$$\frac{2\gamma v_{at}^\beta}{rkT} = (1 - c^p)ln(\frac{1 - c_R^m}{1 - c^m}) + c^p ln(\frac{c_R^m}{c^m}) \tag{A.84}$$

A.4. Single Dislocation Model

In this part, the calculations are given for the single dislocation model (Figure 3.2). Weng et al. [17] proposed a flux going towards the dislocation due to the stress to be J_v and the flux inside the dislocation line towards the particle to be J_d. The diffusion is now described for a cylindrical geometry with different diffusion coefficient inside and outside the cylinder. Inside the dislocation pipe, diffusion is described as

$$\frac{\delta c^p}{\delta t} = D_p \frac{\delta^2 c_d}{\delta z^2} + 2\frac{D_l}{r_0}(\frac{\delta c}{\delta r})|_{r=r_0} \tag{A.85}$$

Where, D_p is the diffusion coefficient inside the dislocation pipe, D_l is the diffusion coefficient in the lattice, c^p is the concentration inside the pipe and C is the concentration in the lattice. Outside the dislocation, diffusion is described as

$$\frac{\delta c}{\delta t} = D_l \frac{\delta}{r\delta r}(r\frac{\delta c}{\delta r}) \tag{A.86}$$

The boundary conditions are

$$c(r,t) = c^\infty, \quad when\ r > r_0\ and\ t = 0 \tag{A.87}$$

$$c(r,t) = c^p(z), \quad when\ r \leq r_0\ and\ t > 0 \tag{A.88}$$

$$c^p(z)|_{z=R} = c^m \tag{A.89}$$

Solving this for a cylindrical coordinate system gives the fluxes J_v and J_d.

$$J_v = -D_l(\frac{\delta c}{\delta r})|_{r=r_0} = \frac{4D_l}{\pi^2 r_0}(c^p - c^\infty)f(t') \tag{A.90}$$

$$J_d = -D_p(\frac{\delta c^p}{\delta z})|_{z=R} = \sqrt{D_p D_l f(t')}\frac{2\sqrt{2}}{\pi r_0}(c^m - c^\infty) \tag{A.91}$$

Where

$$f(t') = \int_0^\infty \frac{exp(-t'x^2)}{x(J_0^2(x) + Y_0^2(x))}dx \tag{A.92}$$

and

$$t' = \frac{D_l t}{r_0^2} \tag{A.93}$$

Where $J_0(x)$ and $Y_0(x)$ are Bessel functions of the first and second kind of the zeroth order. Bessel functions are the solution to the following differential equation.

$$x^2\frac{d^2y}{dx^2} + x\frac{dy}{dx} + (x^2 - \alpha^2)y = 0 \tag{A.94}$$

α is the order the Bessel function and is in this case equal to 0. In the case of positive integers for x and $\alpha = 0$, $J_0(x)$ and $Y_0(x)$ are the following.

$$J_0(x) = \sum_{n=0}^{\infty} (-1)^n \frac{x^{2n}}{2^{2n}(n!)^2} \tag{A.95}$$

$$Y_0(x) = \frac{2}{\pi}((ln(\frac{1}{2}x) + \gamma)J_0(x) + \sum_{k=1}^{\infty} H_k \frac{(\frac{1}{4}(x^2))^k}{(k!)^2}) \tag{A.96}$$

Where H_k is a harmonic number.

$$H_k = \sum_{k_1=1}^{k} \frac{1}{k_1} \tag{A.97}$$

And γ is the Euler-Mascheroni Constant, defined as

$$\gamma = \lim_{k \to \infty}(H_k - ln(k)) \quad or \quad \gamma \approx 0.5772 \tag{A.98}$$

Now, the growth rate due to pipe diffusion can be found by the following mass balance.

$$(c^p - c^m)4\pi R^2 \frac{dR}{dt}|_p = 2\pi r_0 J_d \tag{A.99}$$

This gives

$$\frac{dR}{dt}|_p = \frac{c^\infty - c^m}{c^p - c^m} \frac{\sqrt{2}r_0}{\pi R^2} \sqrt{D_p D_l} \sqrt{f(t')} \tag{A.100}$$

A.5. Boundary Assisted Growth Model

In this part, the calculations are given for the boundary model (Figure 3.3) from Cheng et al. [19]. They proposed that the precipitate is represented by a sphere located in the middle of a thin disk, which represents the boundary. It is assumed that the diffusion in the sphere is rapid so that the spherical shape is maintained. The concentration profile in the boundary is determined by the conversation of mass in the volume element, illustrated in Figure 3.3.

$$N_r - N_{r+dr} - dN_c = dN_b \tag{A.101}$$

Where

$$N_r = -D_b A_c \frac{\delta c_b}{\delta r} \tag{A.102}$$

And

$$dN_b = \delta A_c \frac{\delta c_b}{\delta t} \tag{A.103}$$

Next, dN_c is approximated as [23]

$$dN_c \approx \frac{4D}{d_0}(c_b - c^\infty)dA_s \tag{A.104}$$

Where D_b is the diffusion coefficient in the boundary, A_c is the cross section area, dA_s is the surface area of the volume element, c_b is the concentration profile of the solute inside the boundary, δ is the boundary thickness and d_0 is the average grain diameter. A_c and dA_s are given by

$$A_c = 2\pi r \delta \tag{A.105}$$

$$dA_s = 2\pi r dr \tag{A.106}$$

Assuming that $\frac{dr}{\delta} \approx 1$, the mass balance from equation (A.101) gives

$$D_b(\frac{\delta^2 c_b}{\delta r^2} + \frac{1}{r}\frac{\delta c_b}{\delta r} - \frac{4D}{d_0 D_b \delta}(c_b - c^\infty)) = \frac{\delta C_b}{\delta t} \tag{A.107}$$

Solving equation (A.107) with the following boundary conditions

- $c_b = c^\infty$ when $r << R$
- $c_b = c^m$

This gives the solute concentration profile in the boundary.

$$c_b = \frac{c^m - c^\infty}{K_0(\beta R)} K_0(\beta r) + c^\infty \tag{A.108}$$

Where

$$\beta = \sqrt{\frac{4D}{D_b \delta d_0}} \tag{A.109}$$

The modified Bessel function ($K_0(x)$) is approximated as

$$K_0(x) \approx \sqrt{\frac{\pi}{2x}} e^{-x} \tag{A.110}$$

According to Cheng et al. [19], this gives an error of less then 10 pct. The mass balance can be rewritten as

$$-4\pi R^2 (c^p - c^m) da = (-4\pi R^2 D \frac{\delta c}{\delta r}|_{r=R} - 2\pi R \delta D_b \frac{\delta c_b}{\delta r}|_{r=R}) dt \tag{A.111}$$

Next, equation (A.108) and (A.111) with previous results by Cheng et al. [19] gives the growth rate.

$$\frac{dR}{dt}|_{th} = \Omega(\frac{D}{R} + \frac{\delta D_b}{4R^2} + \frac{\delta D_b \beta}{2R} + (\frac{D_b}{\pi t})^{\frac{1}{2}}) \tag{A.112}$$

In this work, Cheng used the invariant size approximation [9]. The invariant size approximation is an approximation to predict the parabolic growth constant (λ) with a given supersaturation (Ω) just like the concentration profile approximations discussed in this thesis work. We will not go into detail for the invariant size approximation as it is beyond the scope of this thesis work. When using the invariant size approximation under the assumption of a steady state, this gives

$$\frac{dR}{dt}|_{l} = \Omega(\frac{D}{R}) \tag{A.113}$$

Subtracting equation (A.113) from (A.112) gives the growth rate from the boundary

$$\frac{dR}{dt}|_{b} = \Omega(\frac{\delta D_b}{4R^2} + \frac{\delta D_b \beta}{2R} + (\frac{D_b}{\pi t})^{\frac{1}{2}}) \tag{A.114}$$